# Transient Displacement of Newtonian Liquids By Gas in Periodically Constricted Tubes

**Yannis Dimakopoulos and John Tsamopoulos**
Laboratory of Computational Fluid Dynamics, Dept. of Chemical Engineering, University of Patras, Patras 26500, Greece

*DOI 10.1002/aic.10889*
*Published online June 2, 2006 in Wiley InterScience (www.interscience.wiley.com).*

*The displacement of viscous liquids by pressurized gas from harmonically undulated tubes of finite length is examined. This unsteady process gives rise to a long open bubble of varying radius, increasing length and surrounded by the liquid. In general, the thickness of the liquid film that remains on the tube wall is nonuniform. Under creeping flow conditions, it varies periodically, but with a phase difference from the tube radius. The liquid fraction remaining in each periodic segment of the tube increases as the ratio between the minimum and maximum of the tube radius* S *decreases, whereas it tends to the well-known asymptotic value for straight tubes as* $S \rightarrow 1$*, or as the wavelength of the tube undulation increases, although here the flow is accelerating. At high-values of the Reynolds number, the film thickness increases with the axial distance, and the periodicity of the flow field ahead of the bubble tip, which exists under creeping flow conditions, is broken. At even higher Reynolds numbers, recirculating vortices develop inside each tube expansion and when* S *also decreases significantly, nearly isolated bubbles are formed in each tube segment. The location of the bubble tip can be monitored by examining the time variation of the pressure at the tube wall.* © 2006 American Institute of Chemical Engineers
*AIChE J,* 52: 2707–2726, 2006
*Keywords: Liquid displacement by gas; gas-assisted injection molding; oil recovery; flow in undulated tubes; moving boundary problems; elliptic mesh generation.*

## Introduction

The displacement of a viscous liquid by a gaseous phase is a problem of fundamental importance in the chemical and petrochemical industry. There are many practical applications and physical operations, such as the enhanced oil recovery,[1] the monolith reactors,[2] the pulmonary airway reopening,[3] the gas-assisted injection molding,[4] which have as a common basic feature the effective displacement of a liquid by gas. In the secondary oil recovery, air, steam or surfactants are introduced to displace oil lodged in rock pores. Monolith or honeycomb reactors are used for fast multiphase reactions, such as hydrogenations, due to the achieved enhancement in mass-transfer rates. During breathing, air or medication are driven into the lungs and the bronchioli, to expand them and retard or eliminate liquid bridging, which may lead to airway compliant collapse. The gas-assisted injection molding process (GAIM) is a modification of the conventional injection molding technique[5] in which highly pressurized air or inert gas (usually $N_2$) is used to partially displace a molten polymer from a mold and produce hollow plastic articles. This leads to a reduction in the consumed energy for the process and improvement in the quality of the final product.

Because of its importance, the liquid displacement by pressurized gas from circular or noncircular tubes has attracted the interest of many researchers since early last century.[6-13] Invariably, in these theoretical or experimental studies the tube was much longer than its radius and the bubble that the gas formed while displacing the liquid was considered semi-infinite (that is, straight and open in its upstream side), making the motion steady. In particular, Taylor's experiments[8] uncovered important aspects of this problem under creeping flow conditions, such as the three different flow patterns that can arise ahead of the bubble, and the variation of the thickness of the remaining liquid film as a function of the capillary number (*Ca*). Cox[9,10] extended Taylor's measurements at higher capillary numbers

(~10), and showed that the asymptotic value of the volume of the liquid left on the wall of the horizontal cylindrical tube was 0.60. Another noticeable feature of these experiments was the persistent stability of the bubble profile: within a few tube diameters from the entrance, its profile attained an axisymmetric shape with a round-ended tip, which it retained during the rest of its motion down the tube. In their more recent work, Kolb and Cerro[11] examined the evolution of the fluid-fluid interface both in the plane along the axis and normal to it for a wide range of *Ca* numbers in tubes of circular and square cross section. Coating of square capillaries displayed similar phenomena, such as the three types of streamline patterns depending on the value of *Ca*. As expected, the square cross section became more important as *Ca* was lowered.

The first theoretical prediction of the thickness of the wetting film and the pressure drop across a long bubble in a circular capillary tube at very low-capillary numbers was made by Bretherton[12]. His asymptotic method and results were extended by several researchers who employed higher-order theory, examined the effect of surfactants or of the London dispersion forces or the roughness of the tube.[14-19] On the other hand, Bretherton's model inspired others to attack numerically the same problem,[13,20] who used either finite differences or finite elements to solve the Stokes equations in a planar geometry or in a circular tube. At that time, their efforts introduced interesting features about the discretization of the physical domain and the solution procedure of the nonlinear system of equations. Both reproduced Taylor's results for a wide range of capillary numbers. More recently, Giavedoni and Saita[21] reported numerical solutions which included inertia, to an extend limited by the value of *Ca*. They employed an algebraic method to discretize the domain based on spines and they found a nonmonotonic variation of the film thickness as *Re* increased, but only for capillary values larger than 0.05.

Motivated by the need to simulate the gas-assisted injection molding process accurately and efficiently, Dimakopoulos and Tsamopoulos[22] developed and applied a quasi-elliptic mesh-generating scheme for the transient displacement of viscous fluids that obey the Navier-Stokes equations in straight and suddenly constricted tubes of finite length. However, GAIM takes place at much higher driving pressure differences resulting in higher velocities and effective Ca $>$ 10. Their results gave a complete picture of the dynamic evolution of the bubble surface and flow field ahead and behind its tip. In straight tubes, they verified Cox's experimental observations in the high *Ca* and low *Re* regime, whereas they predicted that at high *Re*, in addition to the nonuniformity of the film thickness, a Rayleigh-Taylor instability develops leading to splitting of the bubble tip. Their scheme proved so generic that was successfully applied to the displacement of viscous, viscoplastic and viscoelastic liquids inside tubes with a sudden expansion or enlargement that initially could even be only partially filled with the liquid.[23-25]

The tortuous paths in rock pores, packed beds and lung bronchioli are more complicated than a single straight tube, which has been studied so extensively. Numerous researchers have approximated this randomly varying geometry with a tube with sinusoidally varying cross-section for simulating the single-phase flow of Newtonian and even non-Newtonian fluids.[26] However, studies with two-phase flow are rather limited. For example, Kouris and Tsamopoulos[27-29] have examined the linear stability and the nonlinear dynamics of core-annular liquid-liquid flow and Gauglitz and Radke[30] have examined the penetration of a long bubble through a liquid-filled tube with a single constriction. Although flow in the periodically undulated tube geometry cannot describe latitudinal dispersion in a bed or the exchange of fluid between nearby conduits, it simulates the converging-diverging character of each path in an actual packed-bed, which is important, but cannot be described by a straight tube. On the other hand, the mold geometry in GAIM varies also, but according to manufacturer's needs for the shape of the final article. Here we chose to study the more complicated, but periodic geometry of the tube. We opted to examine the effect of the number of tube undulations, keeping them always more than one, and to allow for straight introductory and exit segments in order to avoid making the usual assumption that the solution is necessarily periodic between each undulation. Our results suggest that indeed the number of tube segments do play a role on the film thickness deposited on the wall, especially when the Reynolds number increases. Moreover, it is shown that monitoring the time variation of the pressure one can determine the location of the front of the penetrating gas and that this arrangement may provide a well-controlled method to produce a stream of bubbles of desired size and frequency.

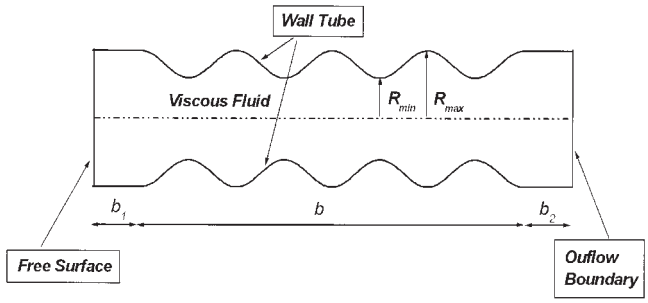


**Figure 1. Flow geometry, an undulated tube, initially completely filled with a Newtonian fluid.**

The evolving fluid domain is discritized into triangular elements via our quasi-elliptic scheme for mesh generation.

## Problem Formulation

We consider the displacement by highly pressurized air of a liquid with constant dynamic viscosity $\mu$ and constant density $\rho$. Figure 1 illustrates the typical flow geometry examined herein. The tube consists of three parts: an introductory segment, a harmonically varying middle part and an exit segment. As indicated earlier we decided to have a number of repeated units in order to determine the conditions under which the flow and the deposited film cease to be periodic, while the introductory and exit segments are necessary in order to accommodate the entrance and exit boundary conditions in the flow field. The lengths of the introductory, middle and exit segments of the tube are $b_1$, $b$ and $b_2$, respectively. The wavelength of the undulation is $\lambda$ resulting in such repeated units in the middle segment, $n = b/\lambda$. The maximum and the minimum radii are equal to $R_{max}$ and $R_{min}$, respectively, with ratio $S = R_{min}/R_{max}$, resulting in the following variation of the tube radius given by the continuous function, $S_r$

$$S_r(\bar{Z}) = \begin{cases} R_{max}, & 0 \le \bar{Z} \le b_1 \\ \dfrac{R_{max}}{2}\left[(1+S) + (1-S)cos\left(\pi\left(2\,\dfrac{\bar{Z}-b_1}{\lambda}\right)\right)\right], & b_1 \le \bar{Z} \le b_1 + b \\ R_{max}, & b_1 + b \le \bar{Z} \le b_1 + b + b_2 \equiv L \end{cases} \quad (1)$$

The viscous liquid initially occupies the entire inner volume of the tube. A step change in the air pressure $\bar{P}air$, is applied on the free surface of the liquid located in the entrance (left-side) of the tube. In particular, at $\tau = 0^+$ the pressure is increased to $\bar{P}_{ext}$: $\bar{P}_{air} = \bar{P}_{ext}H(\bar{\tau})$, where $H(\bar{\tau})$ denotes the Heaviside or step function. The pressure difference between the left entrance and the right exit of the tube ($\bar{P}_{exit} = const < \bar{P}_{ext}$) generates a pressure gradient within it, which drives the liquid to the right and deforms the air-liquid interface forming an open bubble with a constantly increasing length. The air-liquid interfacial tension is $\sigma$. Even though the applied pressure difference remains constant throughout the simulation, the volume of liquid remaining in the tube decreases, reducing the resistance to flow and resulting in an accelerating flow field. Therefore, no steady velocity exists, but a characteristic velocity can be defined, based on the applied pressure difference and resorting to the corresponding Poiseuille flow in a straight completely filled tube of the same total length $L$, $v_{ch} = R_{max}^2\bar{P}_{ext}/(\mu L)$. Scaling lengths with the maximum tube radius $R_{max}$, and stresses with $R_{max}\bar{P}_{ext}/L$, we obtain the following dimensionless parameters: the modified Reynolds number $Re_p = \rho R_{max}^3\bar{P}_{ext}/(L\mu^2)$, the dimensionless external pressure (or modified capillary number) $Ca_p = R_{max}^2\bar{P}_{ext}/(\sigma L) = P_{ext}$, and the aspect ratios $\varepsilon = R_{max}/L$, $\varepsilon_i = b_1/R_{max}$, $\varepsilon_e = b_2/R_{max}$. The subscript $p$, indicates that the definitions of the dimensionless numbers are based on the externally applied pressure, the overbar indicates that the corresponding variable (time, position vector, velocities and pressure) are dimensional. Because of its definition, $Ca_p$ does not involve the liquid viscosity, indicating that it should be better called dimensionless pressure drop. Table 1 summarizes typical values of the dimensional physical properties and conditions that are employed in GAIM, and the corresponding range of dimensionless groups.

**Table 1. Typical Dimensional Parameters and Dimensionless Groups with Representative Values for the Gas-Assisted Injection Molding Process**

| Parameter (Units)/Dimensionless Group | Symbol (Definition) | Value |
|---|---|---|
| Fluid density (kg/m$^3$) | $\rho$ | $\le 10^3$ |
| Fluid viscosity (Pa · s) | $\mu$ | $10^3$–$10^4$ |
| Interfacial tension (N/m) | $\sigma$ | $\le 0.025$ |
| Externally applied pressure (Pa) | $\bar{P}_{ext}$ | $10^5$–$10^7$ |
| Modified Reynolds number | $Re_p = \dfrac{\rho a^3\bar{P}_{ext}}{L\mu^2}$ | $10^{-2}$–$10^{-1}$ |
| Dimensionless external pressure | $P_{ext} = \dfrac{a^2\bar{P}_{ext}}{L\sigma}$ | $10^3$–$10^5$ |
| Total length of the tube | $\varepsilon^{-1} = L/R_{max}$ | $>10$ |
| Undulation ratio | $S = R_{min}/R_{max}$ | 0.–1. |
| Aspect ratio of introductory tube | $\varepsilon_i = b_1/R_{max}$ | $\sim 0.1\varepsilon^{-1}$ |
| Aspect ratio of exit tube | $\varepsilon_e = b_2/R_{max}$ | $\sim 0.1\varepsilon^{-1}$ |

Inserting these characteristic quantities into the radial and axial momentum balances and the incompressibility constraint, we obtain

$$Re_p\frac{D\underline{v}}{D\tau} + \frac{1}{\varepsilon}\nabla P - \nabla\cdot\underline{\underline{\tau}} = 0 \quad (2)$$

$$\nabla\cdot\underline{v} = 0 \quad (3)$$

where $\underline{\underline{\tau}}$ is the viscous part of the total stress tensor $\underline{\underline{\sigma}}$, which is defined as

$$\underline{\underline{\sigma}} = -P\underline{\underline{I}} + \underline{\underline{\tau}} = -P\underline{\underline{I}} + \nabla\underline{v} + (\nabla\underline{v})^T \quad (4)$$

and $\underline{v} = v_r\underline{e}_r + v_z\underline{e}_z$ is the velocity field, $D/D\tau = \varepsilon(\partial/\partial\tau) + \underline{v}\cdot\nabla$ the material derivative, $\nabla = (\partial/\partial R)\underline{e}_r + (1/R)(\partial/\partial\Theta)\underline{e}_\theta + (\partial/\partial Z)\underline{e}_z$ the gradient operator and $P$ denotes the pressure field.

Along the free surface, the velocity field should satisfy a local force balance between viscous stresses $\underline{n}\underline{\underline{\sigma}}$, surface tension $(2H/P_{ext})\underline{n}$, and gaseous pressure $(1/\varepsilon)\underline{n}$:

$$\underline{n}\underline{\underline{\sigma}} = \frac{2H}{P_{ext}}\underline{n} - \frac{1}{\varepsilon}\underline{n} \quad (5)$$

In Eq. 5, $2H$ is twice the local mean curvature of the moving liquid-air interface, $\underline{n}$ is its outward unit normal. The velocity field must be also bounded at the centerline

$$\underline{n}\cdot\underline{v} = 0,\ \underline{t}\underline{n}:\underline{\underline{\sigma}} = 0 \quad (6)$$

zero along the entire tube wall,

$$v_r = 0,\ v_z = 0 \quad (7)$$

and fully developed far downstream[22,23]. To complete the mathematical formulation of the process we assume that initially there is no flow $\underline{v}(R, Z, 0) = 0$, the pressure is uniform $P(R, Z, 0) = 0$ and the liquid surface in contact with the air flat.

## Numerical Solution

### *Elliptic grid generation*

In order to accurately and efficiently solve these equations, we have chosen the mixed finite element method to discretize the velocity and pressure fields, together with a system of quasi-elliptic partial-differential equations, capable of generating a boundary-fitted discretization of the highly deforming

domain occupied by the liquid. We have developed and applied this scheme in order to study the displacement of Newtonian and non-Newtonian liquids inside straight or suddenly constricted or expanding tubes.[4,22-25] It has proved to be superior over previous ones,[31-33] since it takes into consideration the intrinsic features of the developing surface and the deforming control volume. The set of mapping equations is anisotropic in order to capture the large deformation of the free surface primarily along the axial direction. Here, we slightly modify it, allowing the bubble to move in both directions, radial and axial, as it goes through each constriction and expansion. This mapping from the physical domain ($R$, $Z$) to the computational one ($\xi$, $\eta$), is

$$\nabla \cdot \left( \varepsilon_1 \sqrt{\frac{R_\xi^2 + Z_\xi^2}{R_\eta^2 + Z_\eta^2}} + (1 - \varepsilon_1)\nabla\xi \right) = 0 \tag{8}$$

$$\Delta\eta = 0 \tag{9}$$

where the subscripts $\xi$ $\eta$, indicate partial differentiation with respect to each variable $\nabla$ and $\Delta$ are the gradient and Laplace operators in cylindrical coordinates, respectively, defined in the physical domain, and $\varepsilon_1$ is a weighting parameter adjusted by trial and error to optimize the performance of the scheme. $\varepsilon$ ranges from zero to unity and usually takes value *0.1*. The Laplacian guarantees not only a smooth distribution of the nodal points in the complex tube, but also the uniqueness of the numerical solution, preventing the overlapping between parts of the physical domain. The term under the square root in Eq. 8 enforces orthogonality of the mesh in the physical domain preventing discontinuous slopes near the free surface and assisting in keeping the node distribution along the bubble front optimal. The computational domain is a straight cylinder of radius and length $L$ throughout the simulations, whereas the initial shape of the physical domain is generated by creating a sequence of gradual deformations of the computational domain toward the desired shape of the undulated tube. Direct generation of the physical domain, and the mesh nodes, therein, cannot be done due to failure of the Newton Raphson iterations.

Significant components for the success of this scheme are the boundary conditions that accompany it. In particular, on the free surface the two boundary conditions are the kinematic equation

$$\frac{D\underline{F}}{D\tau} = \underline{v} \tag{10}$$

where is the position vector of the free surface, and the requirement that nodes on the moving interface are distributed as uniformly as possible

$$\frac{d^2 s(\xi)}{d\xi^2} = 0 \tag{11}$$

where

$$s(\xi) = \int_0^\xi \sqrt{w_1 R_\xi^2 + w_2 Z_\xi^2}\, d\xi \text{ and } w_1 + w_2 = 2 \tag{12}$$

is a weighted arc-length of the free surface to account for the very different magnitudes of and arising on the deforming surface. Dimakopoulos and Tsamopoulos[22] have shown that a node equidistribution condition, which implies $w_1 = w_2 = 1$, is inadequate for deep gas penetration simulations. They have also proposed that for simulations in straight tubes $w_1$ must be significantly greater than $w_2$, in order to counterbalance the large difference between the magnitudes of the two spatial derivatives. In particular, when we apply Eq. 12 on the bubble free surface, the weighting factor of the derivative in the radial direction $R_\xi$ remains greater than that of $Z_\xi$ as in Dimakopoulos and Tsamopoulos,[22] but their difference is smaller here $w_1 = 1.5$, $w_2 = 0.5$, in order to accommodate the constriction and expansion the tube shape generates on the shape of the developing bubble. On the tube wall and the exit of the tube, the equation that defines the corresponding boundary curve replaces the mesh generation equation associated with the coordinate that is set on that boundary. For the remaining degree of freedom there is a distinction between these two boundaries. On the tube exit, the nodes are distributed uniformly, while relationships (Eqs. 11 and 12) are used for the distribution of the nodes along the wall. The density of the nodes in the expansion and the contraction regions must be higher, so the two weighting factors have been chosen so that $w_1 > w_2$. In this case we observed that the obtained solution converges with mesh faster, if, when we apply Eq. 12 along the sinusoidal wall, we adjust the node distribution by setting these weighting factors on that boundary to $w_1 = 1.2$, $w_2 = 0.8$. This entire procedure generates the node locations, which are connected to form rectangles. However, we have observed that, due to the large deformations of the physical domain, it is better to split each rectangle to form two triangles, which are allowed the deform more without causing any problems in the Jacobian of the transformation to the unit element.

## Implementation of the Mixed Finite Element Method

All the governing equations are approximated using the finite element method according to their individual characteristics. As shown by Kouris et al.[34] the mixed finite element method is accurate and stable for Newtonian fluids with a rate of convergence that is not affected even when singularities are present in the flow problem. In particular, the momentum and mass balance equations follow a mixed formulation, while the equations of the spatial transformation are approximated by basis functions that belong to the lowest order continuous space. The former combination constitutes a stable approximation, which prevents the spurious "checkerboard" pressure mode. The stability of the solution is ensured by projecting the differential equations on the space that is spanned by the corresponding basis functions according to Galerkin's principle. In each triangular element of the computational domain the velocity vector is approximated with the six-node basis functions $\phi^i$, while the pressure and position vector with the three-node basis functions $\psi^j$. We use the latter basis functions for the position vector, see also Tsiveriotis and Brown,[33] because they

are less restrictive and cover the bulk of the physical space, as well as the quadratic basis functions do. On the other hand, linear basis functions are preferable over quadratic ones because they are more stable for the approximation of hyperbolic equations, such as the time-varying kinematic equation.[35,36] This is well known in viscoelastic flow calculations, where in the hyperbolic constitutive equations, the stresses are approximated by bilinear functions using, for example, SUPG.

Having applied the divergence theorem, the weak forms of momentum (Eq. 2), and mass (Eq. 3), balances are given by

$$\int_{\Omega}\left[Re\,\frac{D\underline{v}}{D\tau}\,\varphi^i+\nabla\varphi^i\cdot\underline{\underline{\sigma}}\right]d\Omega+\int_{\Gamma}[\underline{n}\cdot\underline{\underline{\sigma}}]\varphi^i d\Gamma=0,\quad \text{for } i=1,\ldots,N \tag{13}$$

$$\int_{\Omega}(\nabla\cdot\underline{v})\psi^i d\Omega=0,\ \text{for } i=1,\ldots,M \tag{14}$$

where N and M are the corresponding number of nodes in the grid for the velocity and pressure unknowns, respectively. The boundary integral in the momentum residual vector $\int_{\Gamma}[\underline{n}\cdot\underline{\underline{\sigma}}]\varphi^i d\Gamma$ is split into four terms, each one corresponding to a boundary of the computational domain, and it is either substituted by natural boundary conditions on a free surface, or totally replaced by essential boundary conditions on the tube wall. On the exit boundary the unit normal is equal to $\underline{e}_z$ and the integral becomes $\int_{\Gamma_{out}}[\underline{n}\cdot\underline{\underline{\sigma}}]\varphi^i d\Gamma=\int_0^1[-((\partial v_r/\partial z)+(\partial v_z/\partial r))\underline{e}_r+(P-2(\partial v_z/\partial z))\underline{e}_z]dR$. If the boundary condition is applied in one of the "hard" forms, for example, if the $r$-component of the residuals is replaced by $v_r=0$, and the $z$-component is set to zero because $P=0$ and $\partial v_z/\partial z=0$ there, this often leads to numerical instabilities and inconsistencies as the Reynolds number increases.[37] Instead, we employ a "soft" version of the outflow boundary condition: for the $z$-component we act as stated earlier, whereas for the $r$-component we assume that $\partial v_r/\partial z=0$, but we integrate the $\partial v_z/\partial r$ along the outflow boundary, and we incorporate this boundary term to the bulk equations, keeping the axial velocity as an unknown there.[38] This procedure is conveniently incorporated in the Galerkin/finite element method used here.[24] The boundary integral that arises on the moving air-liquid boundary is treated by splitting the mean curvature multiplied by the normal vector into two parts: one that describes the change of the tangential vector along free surface and another one, where the normal vector is divided by the second principal radius of curvature.[39,40] Similarly, the weak forms of the two components of the mesh-generation equations are

$$\int_{\Omega}\left[\varepsilon_1\sqrt{\frac{R_\xi^2+Z_\xi^2}{R_\eta^2+Z_\eta^2}}+(1-\varepsilon_1)\nabla\xi\right]\nabla\psi^i d\Omega=0,\quad \text{for } i=1,\ldots,M \tag{15}$$

$$\int_{\Omega}\nabla\psi^i\cdot\nabla\eta\,d\Omega=0,\ \text{for } i=1,\ldots,M \tag{16}$$

Equations 13–16 are written in the physical domain with independent variables $R$, $Z$, and transformed to the computational one using the chain rule differentiation.

The set of DAEs are integrated using the backward Euler method combined with a forward one for the prediction of a solution at each new time instant and the adjustment of the time step.[41] The proposed scheme is necessary, since in this case the velocity field exhibits large variations in a short time interval. Initially its acceleration is small, but later on, it increases considerably. If a fixed time step were used, this would remain the smallest that would be able to capture the larger variation. Therefore, the total CPU time would well exceed a day, the execution time now needed.

The resulting set of algebraic equations (2N + 3M in total) is nonlinear and must be solved iteratively. In particular, the complete residual set

$$\underline{R}_{es}(\underline{v},\,p,\,\underline{R})=\underline{0} \tag{17}$$

is solved by a two step Newton-Raphson/Nonlinear Gauss-Seidel (Picard) iteration scheme. First, for a given physical domain $\underline{R}=\underline{R}^{j-1}$, the flow problem (Eqs. 13 and 14) is solved

$$\underline{R}_{es}^{v}(\underline{v}^j,\,p^j,\,\underline{R}^{j-1})=\underline{0}\quad (2N+M\ \text{unknowns}) \tag{18}$$

Second, once velocities and pressure have been calculated, the mesh points are moved according to Eqs. 15 and 16, and their boundary conditions

$$\underline{R}_{es}^{m}(\underline{v}^j,\,p^j,\,\underline{R}^j)=\underline{0}\quad (2M\ \text{unknowns}) \tag{19}$$

and the process is repeated until convergence. The combination of time-step adaptation and Newton-Raphson/Nonlinear Gauss-Seidel process consists a very effective way to decouple and solve this inhomogeneous set of equations. The basic advantage of the method is that it generates much smaller Jacobian matrices, which can be allocated and deallocated whenever desired. The convergence of the whole scheme is ensured by the automatic time adaptation, because the predicted solution does not differ too much from the exact one and the Newton/Kantorovich sufficient condition is satisfied. The approximate CPU-time per time step is of the order of a few minutes — very close to the time that is needed by a full Newton-Raphson scheme. However, the memory savings with this scheme are significant because of the elimination of mixed entries (entries coupling the flow and the mesh generation equations) in the Jacobian matrix.

The entries of each Jacobian matrix are calculated analytically. Convergence is controlled by a prespecified tolerance of $10^{-9}$ for the absolute error norm of the residual vector. Whereas, the prespecified tolerance of the nonlinear Gauss-Seidel process is slightly greater ($0.5\times10^{-8}$), in order to avoid premature termination of the Picard iterations. The nonlinear solver does not need more than five cycles per time step to converge, while the storage requirements are significantly reduced, because each banded Jacobian has a smaller bandwidth. Additional acceleration of the calculations is achieved by applying the chord Newton method: LU decompositions of the Jacobian matrices remain temporarily frozen. The large system

of algebraic equations, which results at each Newton iteration, was solved by direct Gaussian elimination using a band-matrix solver, which allows row and column pivoting. A fine mesh is required, in order not only to capture the flow, but also to resolve the shape of the moving interface accurately. Extensive convergence tests have been undertaken and have shown that unless otherwise stated in the more demanding simulations, the number of nodes that should be used in the radial and axial direction is 47 and 131, respectively. This number of nodes results in 11,960 triangles completely and nearly uniformly covering the entire deforming domain, and in 12,314 equations which are used to determine the node locations, 48,546 equations for the velocity, and 6,157 equations for the pressure unknowns. The program was written in Fortran 90, and was run on an Alpha Dec DS20E workstation at the laboratory of Computational Fluid Dynamics. Depending on the parameters and the kind of geometry, it took about a day to complete a run.

## Results and Discussion

The liquid displacement from a tube of finite length by air depends on the dimensionless numbers stated earlier, and summarized in Table 1, along with their typical values in GAIM. In this section, first we focus on how the computed finger shape, the velocity and pressure fields and some other characteristics of the process depend on this basic set of parameter values and, subsequently, we examine how these process characteristics are affected by changes in parameter values around this base case.

Figure 2 shows snapshots of fluid displacement under creeping flow conditions inside an undulating tube with total dimensionless length equal to $\varepsilon^{-1} = 12$. The lengths of the introductory and the exit tubes are equal to $\varepsilon_i = \varepsilon_e = 1.2$. Numerical experiments have shown that this exit length is sufficient, as it does not affect the flow field, which has become fully developed in this case before the exit plane, even when the bubble front is very close to it (Figure 2e). The spatial wavelength of each undulation is equal to $\lambda = 2.4$, and the ratio of the minimum to the maximum radius is $R_{min}/R_{max} = 0.7$. Finally, the dimensionless applied pressure at the left entrance is $P_{ext} = 8333$. The snapshots show contour lines of the axial (upper half) and radial (lower half) velocity components at five time instances when the bubble tip is at $Z_{tip} = 2$, 4, 6, 8 and 10, respectively. The bubble exhibits a continuous variation of its front, and also its side surface in order either to squeeze through the constrictions of the tube or to expand inside its wider sections. Since the undulation ratio is moderate, the bubble front never becomes too pointed in the process, as it did in a tube with a sudden constriction.[22,23] The remaining film has a nonuniform thickness distribution, being thinner in regions where the tube undergoes expansions, and thicker where the tube undergoes contractions. In other words, after the bubble passes through a constriction, it immediately expands forcing most of the liquid away, but it cannot keep moving parallel to the wall up to the tube crest. Instead, it turns away from the wall leaving a thicker film behind it and, to some extend, bypasses the rest of the undulation reaching the next constriction. Thus, the maxima and minima of the bubble interface arise before the corresponding ones on the wall. Since the bubble acts on the liquid only through its constant pressure, this variation is caused by the relatively small, in this case, capillary force, but mainly by the locally sharper pressure gradient. Both the capillary force and the pressure gradient (see Figure 3) are maximized at a tube constriction leading to minimization of the liquid pressure just ahead of the bubble tip and to the easier removal of liquid by gas. Exactly the opposite occurs at a tube expansion.

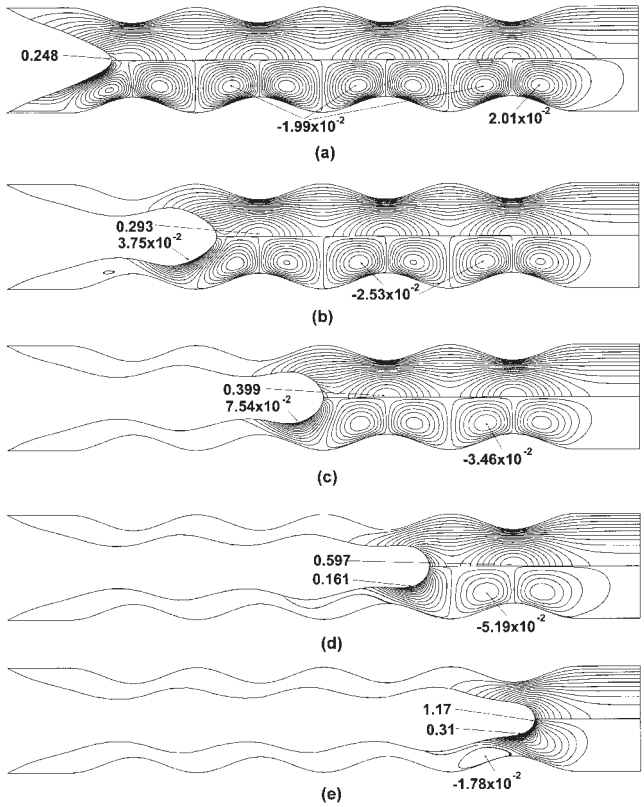


**Figure 2. Contour lines of the axial and radial velocity component, upper and lower part of each figure, in an undulated tube with $R_{min}/R_{max} = 0.7$ at $\tau = 1.06$, 1.72, 2.21, 2.56 and 2.79. ($Re_p$, $P_{ext}$, $\varepsilon^{-1}$, $n$, $\varepsilon_i$, $\varepsilon_e$) = (0, 8333, 12, 4, 1.2, 1.2).**

Returning to Figure 2, we observe that the absence of inertia allows the flow field in the area ahead of the bubble tip and before the last tube expansion to remain symmetric with respect to planes normal to the axis of symmetry at locations, where the tube radius is either minimized or maximized. The radial velocity is always positive around the bubble front as liquid has to be moved aside for the bubble to pass. Further downstream there is a succession of positive (in the expanding section) and negative (in the constricting section) radial velocities. This symmetry of the flow field in each undulation is disturbed only by the presence of the bubble front. In the illustrated snapshots, with the exception of the first one at $\tau = 1.063$, the maximum value of $v_r$ is located on the side of the bubble front, whereas its minimum is always located downstream from the bubble front and before a constriction. Of course, because of the previously mentioned flow symmetry, three and two local minima exist in the first two instances. The figure depicts the positions of the maximum and the minimum values of both velocity components, noting that the minimum of the axial velocity is zero and occurs along the tube wall. The

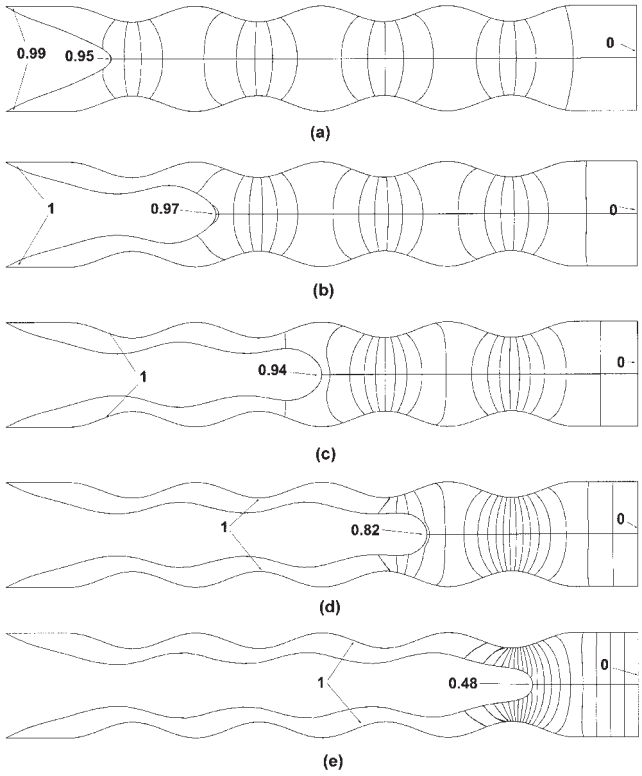


**Figure 3. Contour lines of pressure in an undulated tube with $R_{min}/R_{max}$ = 0.7 at $\tau$ = 1.06, 1.72, 2.21, 2.56 and 2.79. ($Re_p$, $P_{ext}$, $\varepsilon^{-1}$, $n$, $\varepsilon_i$, $\varepsilon_e$) = (0, 8333, 12, 4, 1.2, 1.2).**

contour lines of the axial velocity component follow the variation of the tube wall and exhibit local maxima around the constrictions. The location of the absolute maximum in axial velocity is either at the bubble tip when that is going through a constriction (Figure 2a and 2e), or at the first constriction ahead of the bubble front when the bubble tip is in the wider part of the tube (Figure 2b,c,d). For example, at $\tau = 1.715$ (Figure 2b) the tip velocity is $v_{tip} = 0.266$, whereas the maximum of is $v_z$ 0.293, while at $\tau = 2.211$ (Figure 2c) $v_{tip} = 0.324$ and $max(v_z) = 0.399$. Common feature of both these snapshots is that the bubble front is expanding, and, thus, its instantaneous axial velocity has to decrease.

The pressure distribution in the liquid is shown in Figure 3. The pressure decrease is stronger around the constricted sections, since more energy is consumed there so that the liquid can overcome the constriction. The axial pressure variation resembles compression waves. At the tube exit, the pressure isolines are straight and parallel to each other, intersecting vertically the tube wall. Therefore, the pressure gradient there becomes one-dimensional (1-D), in the axial direction only, and linear even when the bubble front is very close to it (Figure 3e), verifying that indeed the flow is well developed at the exit. Pressure isolines intersect the undulating wall nearly vertically, as well. So they have to bend following the tube geometry. Due to the specific morphology of the wall, the pressure varies on the deposited material for a distance of about a tube diameter behind the bubble tip, something we did not observe in straight tubes. Of course, keeping the pressure constant at the two ends of the tube leads to pressure gradients that increase with time and an accelerating flow.

Figure 4 helps us appreciate quantitatively the axial pressure variation in the tube by showing its values along the wall. Examining first the curve that corresponds to the first time instant ($\tau$ = 1.07), we observe that apparently there is a different variation of the pressure along the three distinct parts of the tube. The pressure drop is a linear function of the axial position in the introductory and the exit sections, and undergoes a smooth and nearly stepwise variation inside the undulating part. The pressure drop inside each undulation filled with liquid equals − 0.238. The pressure drop along the exit tube is significantly greater than that in the introductory tube, because part of the volume of the latter is occupied by gas, and the rest by nearly stationary liquid neither of which consumes energy in the form of pressure loss in order to move. As time increases, the slope of the pressure curves in the introductory tube and the partially gas-occupied undulations decreases (in absolute value), approaching zero and so, in a longer section of the tube wall the pressure approaches 1.0, while, necessarily, the corresponding slope in the exit tube and in the undulations still occupied by liquid increases. The slope in the exit tube takes successively the values −0.042, −0.054, −0.072, −0.109, and −0.276 at the indicated time instants, while its value in each liquid filled undulation changes from −0.302 at =1.715 to −0.414 at $\tau$ = 2.23.

The previous two figures give us only the spatial variation of pressure at given time instants. In experiments, it is easier to record the time-evolution of the pressure at a certain location, and as we will see shortly this can be used to locate the position of the bubble tip. To this end, we have drawn in Figure 5 the tip pressure vs. time, and in Figure 6 the wall pressure, $P_w$ at Z = 6 vs. bubble-tip position. In addition to the tip pressure, in Figure 5 we have included the time evolution of the tip velocity. The initial value of the tip pressure immediately after the beginning of the process is slightly above one, 1.013, for reasons we have explained elsewhere.[23] Up to $\tau$ = 1.0 the

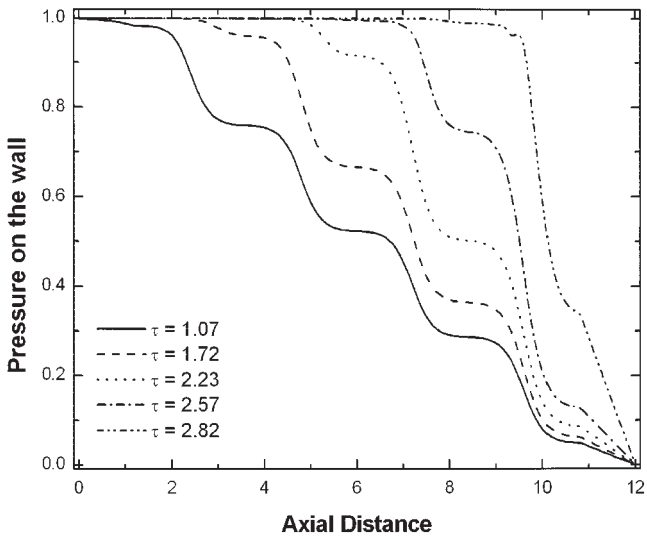


**Figure 4. Pressure distribution on the tube wall at various time instants for ($Re_p$, $P_{ext}$, $\varepsilon^{-1}$, $R_{min}/R_{max}$, $n$, $\varepsilon_i$, $\varepsilon_e$) = (0, 8333, 12, 0.7, 4, 1.2, 1.2).**

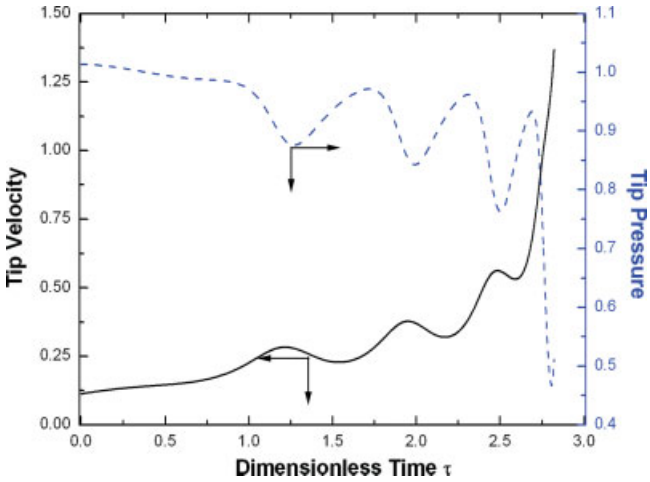


**Figure 5. Evolution of the tip pressure and tip velocity for ($Re_p$, $P_{ext}$, $\varepsilon^{-1}$, $R_{min}/R_{max}$, $n$, $\varepsilon_i$, $\varepsilon_e$) = (0, 8333, 12, 0.7, 4, 1.2, 1.2).**

[Color figure can be viewed in the online issue, which is available at www.interscience.wiley.com.]

pressure declines linearly, but beyond this time it exhibits, in addition to its decline on average, periodic variations with an increasing amplitude and frequency. Table 2 summarizes the values of the temporal maximum and minimum values of the tip pressure and velocity during the whole process. There is a time delay in the response of the pressure at the bubble tip; it has a local minimum or maximum after the bubble front has passed through the tube minimum or maximum, respectively. For example, the bubble reaches at the first constriction at $\tau = 1.142$, and the pressure is minimized at $\tau = 1.269$. On the other hand, the response of the bubble-tip velocity is completely different. It begins with a nonzero initial value, $v_{tip} = 0.113$, because of the absence of liquid inertia, and increases, but nonmonotonically because of the combination of the accelerating nature of the flow and the variable tube radius. The velocity is maximized right after each constriction and minimized right after each expansion. Thus, the response of the velocity is also delayed, but not as much as the pressure.

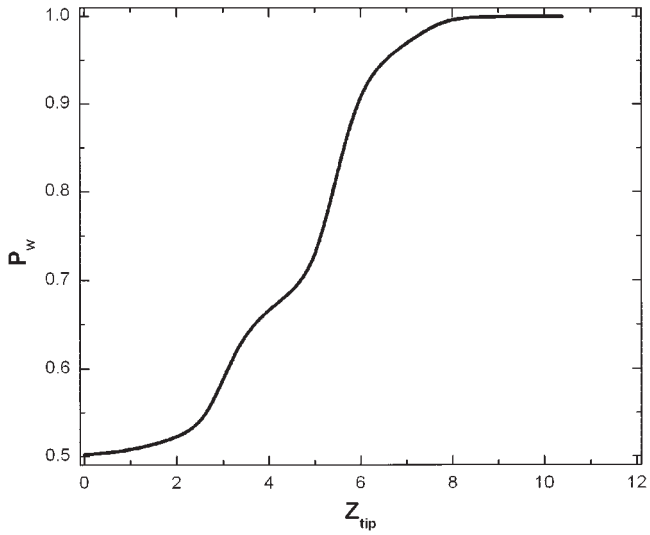


**Figure 6. The evolution of the pressure at the middle of the tube wall as a function of the location of the bubble tip for ($Re_p$, $P_{ext}$, $\varepsilon^{-1}$, $R_{min}/R_{max}$, $n$, $\varepsilon_i$, $\varepsilon_e$) = (0, 8333, 12, 0.7, 4, 1.2, 1.2).**

**Table 2. Temporal Maximum ($M$) and Minimum ($m$) Values of the Tip Pressure and Velocity for $Re_p = 0$, $P_{ext} = 8333$, $n = 4$, $R_{min}/R_{max} = 0.7$ and $\varepsilon^{-1} = 12$**

| Points | Character | Time | Pressure | Velocity |
|---|---|---|---|---|
| 1 | $M$ | 1.215 | — | 0.283 |
| 2 | $m$ | 1.269 | 0.875 | — |
| 3 | $m$ | 1.537 | — | 0.228 |
| 4 | $M$ | 1.721 | 0.971 | — |
| 5 | $M$ | 1.951 | — | 0.377 |
| 6 | $m$ | 1.954 | 0.842 | — |
| 7 | $m$ | 2.171 | — | 0.319 |
| 8 | $M$ | 2.308 | 0.961 | — |
| 9 | $M$ | 2.489 | — | 0.562 |
| 10 | $m$ | 2.504 | 0.763 | — |
| 11 | $m$ | 2.588 | — | 0.531 |
| 12 | $M$ | 2.688 | 0.933 | — |

Although the curve of the time evolution of the pressure on the tube wall at Z = 6 does not exhibit as large variations as the tip pressure, it varies more until the bubble tip passes by this observation position, at which point it starts approaching its asymptote 1. When the process begins, the initial value of the local pressure is nearly 0.5 (0.502), because the point is located in the middle of the tube. Then it starts to increase with a rather small slope until the bubble passes over the first constriction at which instant its slope increases more abruptly. Subsequently, the wall pressure at Z = 6 has a smaller slope until the bubble overcomes the resistance of the second constriction, when another sharp increase in the pressure slope is observed. After that and when the bubble tip reaches the location Z = 6 the pressure takes ~90% of its final value 0.906, and signifies that the bubble tip has passed this observation location. Beyond this instant, the slope of the curve declines steadily and the pressure reaches its final value of 1. This means that the remaining film has taken a permanent shape and is not affected any more by the externally applied pressure.

### *Effect of undulation ratio ($S = R_{min}/R_{max}$)*

The undulation ratio may vary from very small (~0.1) to values up to 1 (then the tube becomes straight) depending on the application that we are interested in. We begin the parametric analysis of the contraction ratio with an interesting observation about the distribution of the remaining material inside undulating tubes under creeping flow conditions ($Re_p = 0$), large values of the externally applied pressure ($P_{ext} = 8333$) and $R_{min}/R_{max} = 0.8$. Figure 7 shows superimposed snapshots of the evolution of the free surface at times that correspond to tip locations $Z_{tip} = 4.056$, 6.015, 8.046, 10.03, and 11.99, as seen in a specific tube section. We observe that the shape of the remaining film is not modified after its width has been adjusted by the passing bubble, despite the constant gas pressure and the accelerating nature of the flow. If we focus on a single undulation, we observe again that the free surface exhibits a quasi-periodic distribution with its crest and trough shifted in the upstream direction with respect to the tube maximum and minimum, respectively. The periodicity of the interface is in

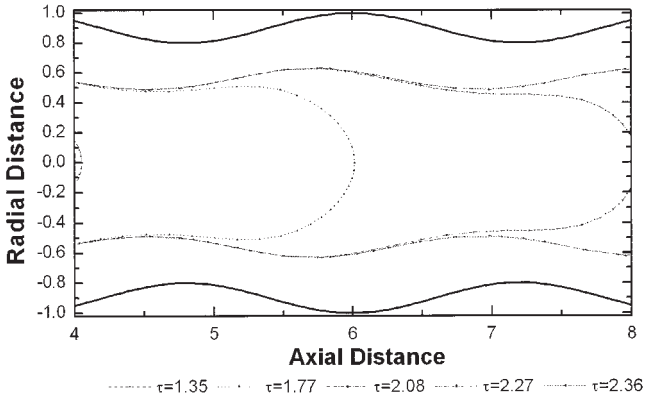


**Figure 7. Close ups of the evolution of a bubble at successive time instants for ($Re_p$, $P_{ext}$, $\varepsilon^{-1}$, $R_{min}/R_{max}$, $n$, $\varepsilon_i$, $\varepsilon_e$) = (0, 8333, 12, 0.8, 4, 1.2, 1.2).**

agreement with previous theoretical studies, which *a priori* assumed periodicity in the steady and transient, core-annular flow of two viscous fluids inside periodically constricted tubes.[27-29]

Figure 8 shows the distributions of the free surface in the second expansion for four tubes with undulation ratios 0.8 (Figure 8a), 0.6 (Figure 8b), 0.4 (Figure 8c), and 0.2 (Figure 8d), under creeping flow conditions. For clarity, the illustrated tube section is slightly longer than the wavelength of a single undulation. All the snapshots correspond to long times for each geometry, so that the remaining film in this section has reached its final thickness. The interfaces are indicated by the dotted lines in which the darker dots correspond to the exact locations of mesh nodes, and the lighter ones to straight line interpolations between them. Comparing first the times on each figure against the nearly equal bubble tip locations in Table 3, we clearly see an increase in the time the bubble needs to go through each constriction as $R_{min}/R_{max}$ decreases. The table also gives the locations and the values of the interface maximum and minimum in each case. In order to determine these values to the indicated accuracy we used least squares, and a fourth-degree polynomial interpolation of eight mesh points that were visibly closest to each extremum in Figure 8. The data in the table indicate that, whereas the location of the crest and the trough of the interface are invariant with $R_{min}/R_{max}$, and upstream with respect to the maxima and minima in the tube radius, their values decrease with the ratio in tube radii and more so the radius at the bubble trough. This is a result of the increased effort by the bubble to pass through a narrower constriction and its inability to expand to the same extend after it does, instead it remains narrower following more closely the path of minimum resistance to the next constriction. Starting from the location downstream from the tube minimum, where the bubble surface has an inflection point and moving in the downstream direction the width of the remaining film increases and begins to decrease only for axial distances greater than ~6.3. The minimum width of the film is located upstream with respect to the interface crest irrespective of the value of $R_{min}/R_{max}$. For example, the minimum width for undulation ratio equal to 0.2 is located at Z ~5.1. From a computational point of view, we see in Figure 8 and Table 3, that as the arc length of the tube wall increases (that is, decreases), the number of

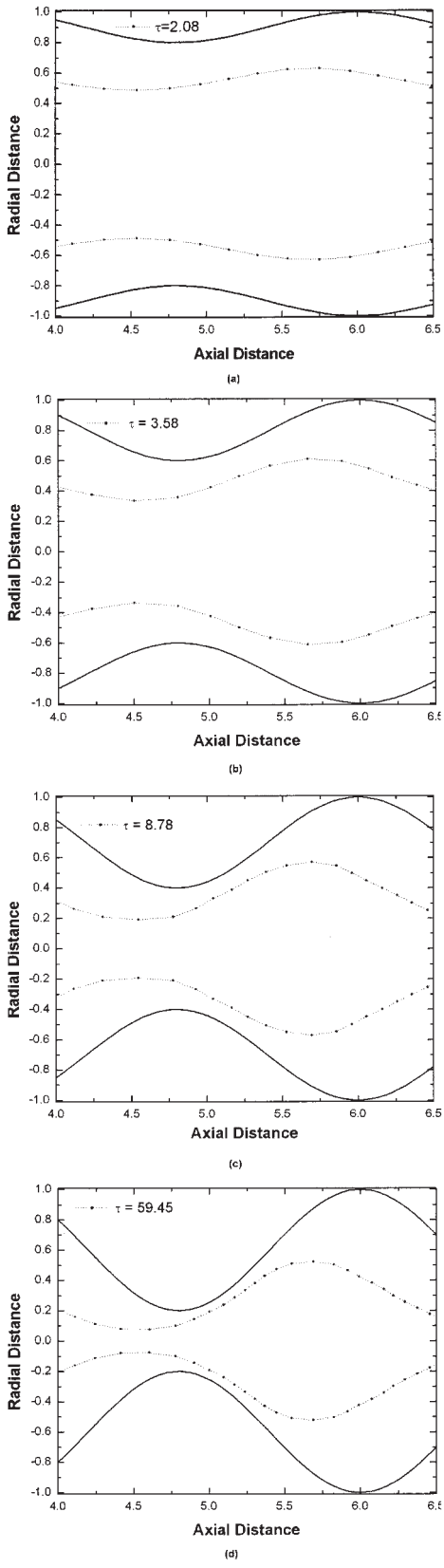


**Figure 8. Effect of $R_{min}/R_{max}$ on the shape of the remaining film for (a) $R_{min}/R_{max}$ = 0.8, (b) $R_{min}/R_{max}$ = 0.6, (c) $R_{min}/R_{max}$ = 0.4 and (d) $R_{min}/R_{max}$ = 0.2 with ($Re_p$, $P_{ext}$, $\varepsilon^{-1}$, $n$, $\varepsilon_i$, $\varepsilon_e$) = (0, 8333, 12, 4, 1.2, 1.2).**

Table 3. Locations and Values of Interface Crest and Troughs and Number of Mesh Points as a Function of $R_{min}/R_{max}$ for $P_{ext} = 8333$, $Re_p = 0$, $\varepsilon^{-1} = 12$

| $S = R_{min}/R_{max}$ | Location of Bubble Tip, $Z_{tip}$ | Minimum | | Maximum | | Mesh Nodes on Interface in Section | Mesh Nodes in the Radial Direction |
|---|---|---|---|---|---|---|---|
| | | Location | Radius | Location | Radius | | |
| 0.8 | 8.046 | 4.540 | 0.487 | 5.708 | 0.628 | 8 | 47 |
| 0.6 | 8.770 | 4.539 | 0.333 | 5.695 | 0.611 | 11 | 47 |
| 0.4 | 8.287 | 4.540 | 0.185 | 5.681 | 0.575 | 18 | 61 |
| 0.2 | 8.078 | 4.540 | 0.070 | 5.689 | 0.524 | 24 | 81 |

nodes needed in each tube section to accurately describe the bubble surface, increases as well. In order to achieve this increase, we had to increase the radial nodes in the computational domain before the start of the simulation resulting in an increase in the computational cost and then allow the mesh generation scheme to allocate them where they are needed the most, that is, where the interface undergoes the most rapid changes.

In addition to the free surface, the undulation ratio affects the distribution of pressure along the tube. In order to demonstrate this, we have computed the fluid pressure on the tube wall at given time instant for zero Reynolds number and several values of $S$, but show them only for the extreme values of $S = 0.9$ and 0.2 in Figure 9. The case with $R_{min}/R_{max} = 0.7$ was discussed in relation to Figure 4. As the ratio $R_{min}/R_{max}$ decreases, the impact of the undulated part of the tube on the evolution of the bubble becomes more significant than that of the introductory or the exit sections of the tube. This is apparent even in Figure 4, where we observe that the variation of the pressure gradient inside the introductory tube is nearly zero for all times, while inside the exit tube is low except when the bubble tip has come very close to it. For undulation ratio 0.9 (Figure 9a), the pressure exhibits small amplitude oscillations superimposed on a linear decrease, which becomes sharper with time. The steeper gradient at time $\tau = 0.64$ is equal to $-0.137$, and occurs in the second constriction. As the part of the tube, which is occupied by air increases, a larger portion of a pressure curve approaches a zero slope, and the steepest gradient approaches its value in the tube exit. On the other hand, when $S = 0.2$, the pressure undergoes nearly step changes in each undulation from the very beginning, with sharp decreases in each constriction still occupied with liquid to be displaced.

Changes in $R_{min}/R_{max}$ affect the bubble tip and tube outflow velocity, as well. Figure 10 shows simultaneously their time evolution for four values of $R_{min}/R_{max}$ (a) 0.9, (b) 0.6, and (c) 0.2. Both velocities are represented by the corresponding capillary numbers, and their values are obtained from $Ca_{tip} = P_{ext} v_{tip}$, for example. This makes plain that due to the accelerating character of the flow, the usual dimensionless parameters, such as $Ca_{tip}$, are not constant. In the last two cases, the number of radial elements has been increased, as indicated in Table 3. For $R_{min}/R_{max} = 0.9$, Figure 10a, the response of the two velocities is similar to that in a straight tube,[22] since the amplitude of the wall undulation is small. Both velocities increase slowly with time, until the time the bubble tip is near the tube exit, when a steep increase by almost an order of magnitude in velocities is seen. Superimposed on these curves one may observe small amplitude variations, which are caused by the small undulations of the free-surface during its development. The initial values of $Ca_{tip} = 1660.9$ and $Ca_{out} = 1736.5$ differ by about 5%. However, the mean acceleration of the bubble tip is higher than that at the outlet, and the velocity at the outlet is less sensitive to temporal variations of the flow. At time $\tau \sim 2$, the bubble comes close to the exit and both quantities increase by more than an order of magnitude. The simulation stops when the bubble approaches the outflow boundary Z = 11.999 at $\tau = 2.049$. As $R_{min}/R_{max}$ decreases, the

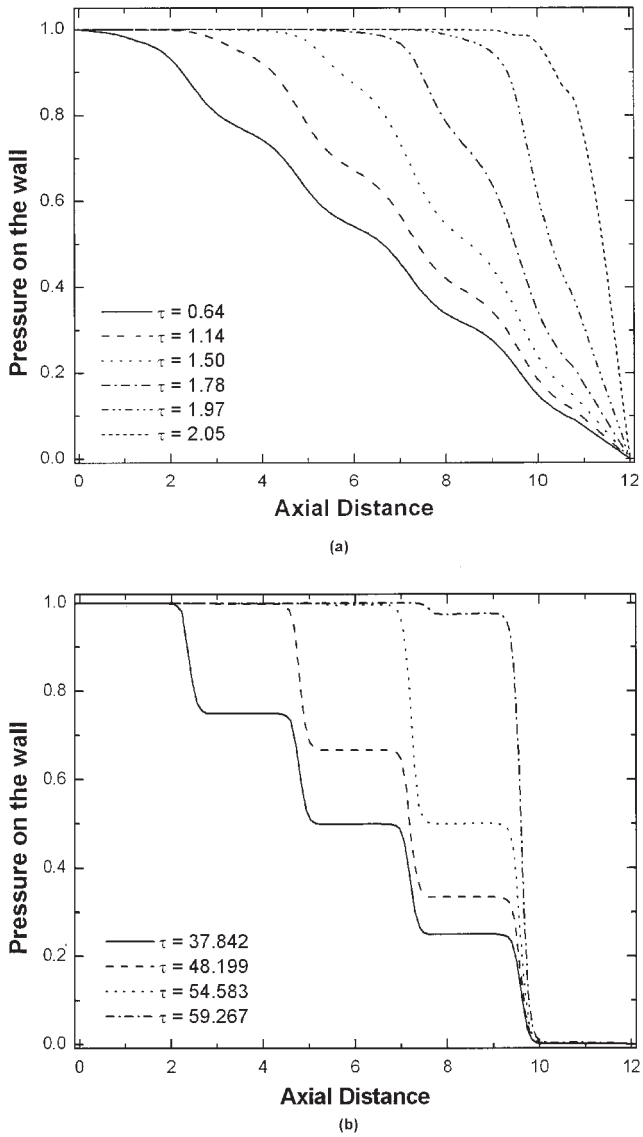


Figure 9. Effect of the tube undulation ratio on the pressure distribution on the tube wall for (a) $R_{min}/R_{max} = 0.9$ and (b) $R_{min}/R_{max} = 0.2$ with ($Re_p$, $P_{ext}$, $\varepsilon^{-1}$, $n$, $\varepsilon_i$, $\varepsilon_e$) = (0, 8333, 12, 4, 1.2, 1.2).

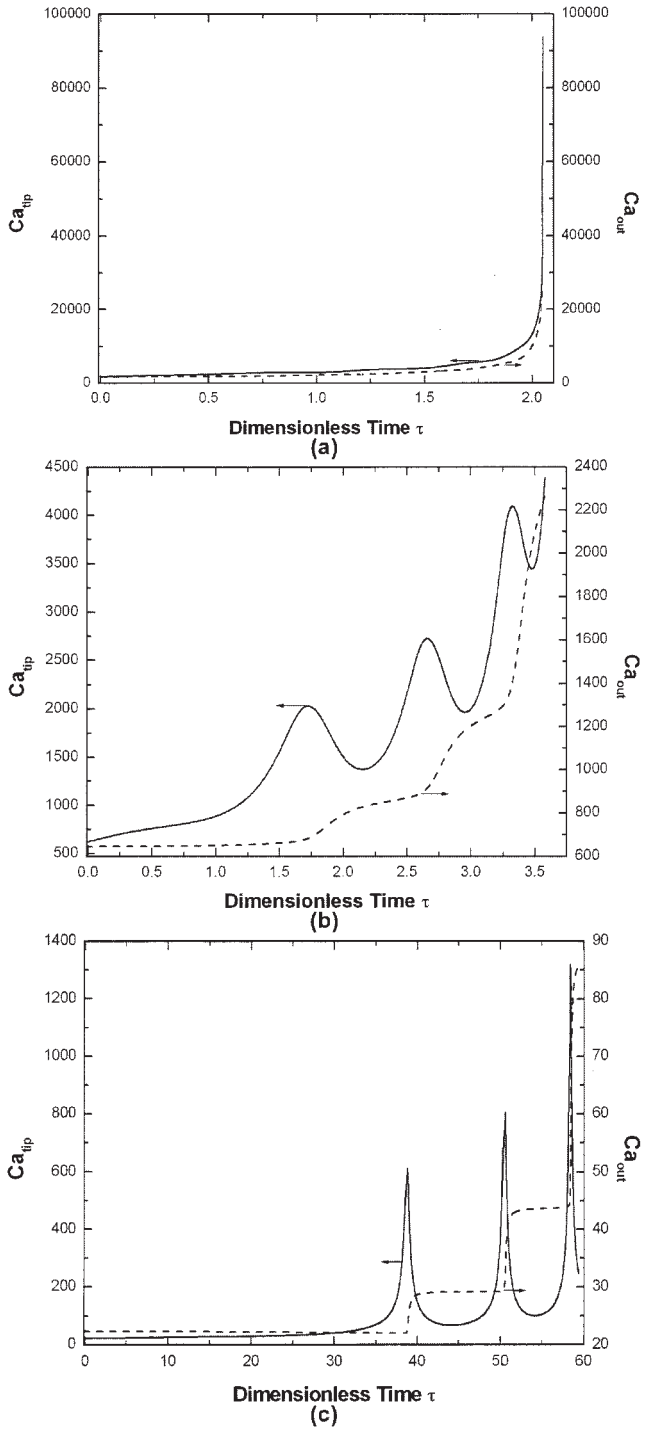


**Figure 10. Effect of the tube undulation ratio on both the time variation of the velocity of the fingertip ($Ca_{tip}$) and the velocity at the centerline of the outlet boundary ($Ca_{out}$) (a) $R_{min}/R_{max}$ = 0.9, (b) $R_{min}/R_{max}$ = 0.6 and (c) $R_{min}/R_{max}$ = 0.2 with ($Re_p$, $P_{ext}$, $\varepsilon^{-1}$, $n$, $\varepsilon_i$, $\varepsilon_e$) = (0, 8333, 12, 4, 1.2, 1.2).**

difference between the responses of the two velocities becomes more apparent. In particular, for $R_{min}/R_{max}$ = 0.6, the tip velocity takes initially a smaller, nonzero value ($Ca_{tip}$ = 616.8), increases until reaching a local maximum at $\tau = 1.722$, then it decreases until reaching another local minimum, and so on. The bubble motion is decelerated and accelerated whenever the bubble is going through a constriction or an expansion in the tube (particular values from this and other figures, herein, are available upon request from the authors). In contrast, the outlet velocity, measured as $Ca_{out}$ exhibits a different response to the variations of the tip velocity. Its initial value is 644.82, about 5% larger than the tip velocity and its increase is monotonic, but its acceleration changes from low to high periodically. The maxima in the evolution of the tip velocity are immediately followed by temporary increases of the acceleration in the outlet, whereas after the tip velocity minima, the acceleration of the outlet velocity decreases, always remaining positive. A further decrease in the undulation ratio, $R_{min}/R_{max} = 0.2$ intensifies these features of the bubble tip velocity inside the sinusoidally varying segment of the tube, making the peaks narrower and steeper. On the other hand, the variations of the outlet velocity resemble those of a system that undergoes stepwise increases. In fact, we may conclude that the coupled system of $Ca_{tip}$,$Ca_{out}$, for small values of $R_{min}/R_{max}$ tends to respond in a rather simple way. The tip velocity approaches a sequence of Dirac delta functions ($\delta(\tau - \tau_0)$), while the signal at the outflow boundary consists of the time-integrated responses of these functions. In other words, $Ca_{out}$ follows the Heaviside function $H(\tau) = \int_0^\tau \delta(\tau')d\tau'$.

Figure 11 shows that the bubble tip moves toward the tube exit monotonically and, of course, each time the tip velocity has a maximum as the bubble front passes through a constriction, it is displaced faster. This effect becomes more pronounced as $S$ decreases, and it is shown here for $S = 0.2$. This picture is very similar to the one reported by Gauglitz and Radke.[30] There it was shown theoretically and experimentally that as the bubble was going through a single constriction its front would undergo either a dumped oscillation or a step increase depending on whether the Ohnesorge number ($Oh = \mu/(\rho R_{max}\sigma)^{0.5} = (P_{ext}/Re_p)^{0.5}$) was below or above 0.02. In

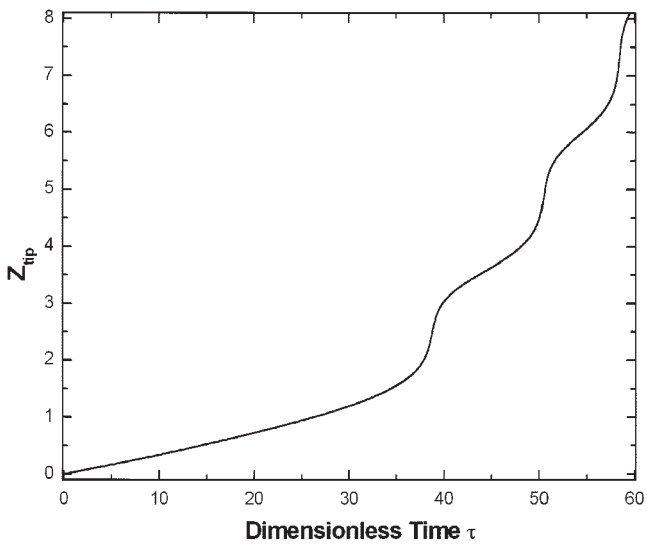


**Figure 11. Evolution of the bubble tip location with ($R_{min}/R_{max}$, $Re_p$, $P_{ext}$, $\varepsilon^{-1}$, $n$, $\varepsilon_i$, $\varepsilon_e$) = (0.2, 0, 8333, 12, 4, 1.2, 1.2).**

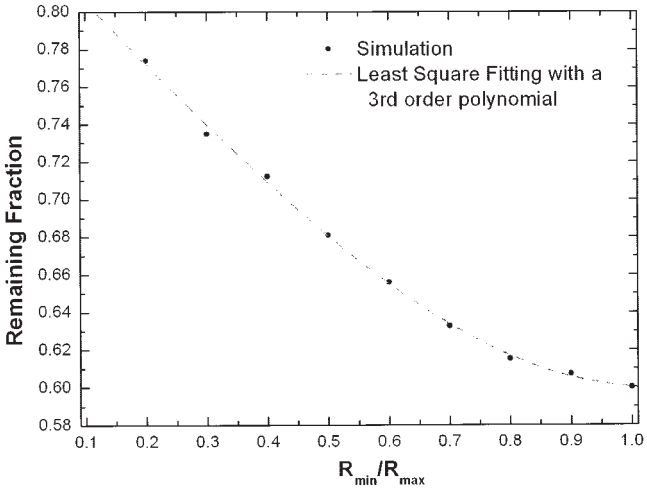


**Figure 12. Remaining liquid fraction on the tube walls vs. the undulation ratio ($Re_p$, $P_{ext}$, $\varepsilon^{-1}$, $n$, $\varepsilon_i$, $\varepsilon_e$) = (0, 8333, 12, 4, 1.2, 1.2).**

Also shown is a best fit to the points by a third-degree polynomial $m_p = 0.8385 - 0.3287(R_{min}/R_{max}) - 0.0398(R_{min}/R_{max})^2 + 0.1303(R_{min}/R_{max})^3$.

all the results presented herein, $Oh>0.02$. A very similar prediction has been reported by Staples and Shaffer.[42]

An important result of these simulations is the determination of the volume of remaining liquid in each undulation during this gas-assisted displacement from the interior of a tube, and its dependence on the ratio. This amount is defined as

$$m = 1 - \frac{\int_0^{\lambda} R^2(Z)dZ}{\int_0^{\lambda} S_r^2(Z)dZ} \tag{20}$$

and as seen in Figure 12, its value increases, *as* $R_{min}/R_{max}$ decreases. Of course its value for *as* $R_{min}/R_{max} = 1$ coincides with the result for a straight tube, $m = 0.595$.[8,23] The increase in the remaining liquid fraction results from the smaller decrease in the crests and troughs in the bubble wavy side surface as $R_{min}/R_{max}$ decreases, and, thus, from the increased tendency of the bubble to avoid sweeping the liquid from the wider parts of the tube. Characteristically, the relative increase of $m$, when $R_{min}/R_{max}$ decreases from 0.7 to 0.4, is equal to 12.1%. It must be noted that these calculations are based on integrating a fourth-degree polynomial interpolation of sequences of eight mesh points on the free surface, which was obtained using least squares.

### *Effect of the Reynolds number*

Inertia is an important factor in the dynamics of the displacement process. We have already shown[22,23] that in straight tubes inertia controls the thickness distribution of the remaining film, the evolution of both the tip velocity and the velocity at the exit boundary, and so on. In order not to increase substantially the length of the exit tube every time we increase $Re_p$ and then have to check that the results are independent of it, we employ the "soft" boundary conditions at the exit and keep both velocities as unknowns there.[38] It is well known that this technique is even more suitable for parabolic problems, since in such problems any information propagates mainly in the downstream direction.

Figure 13 depicts the evolution of the free-surface for three values of the pressure-based Reynolds number (a) $10^2$, (b) $10^3$, and (c) $5 \times 10^3$. The total dimensionless length of the tube is 12, and the undulation ratio of the wall is $R_{min}/R_{max} = 0.8$. Beginning with Figure 13a, we conclude that up to $Re_p = 100$ the effect of inertia is not very significant, with the exception of the bubble front at early times $\tau = 1.85$, which is wider than in the case with $Re_p = 0$. At the initial stages of the bubble penetration, its front is almost flat and tends to displace more of the material that initially occupies the introductory tube producing a thinner film. However, this is limited only to its motion in the introductory tube. After the bubble tip reaches the first constriction, the locally increased inertia (the axial velocity is maximized there) forces the bubble to partially bypass the next widening in the tube, and its side interface does not follow closely the variations of the tube wall even as the tube radius increases. This is opposite to the recurring theme in

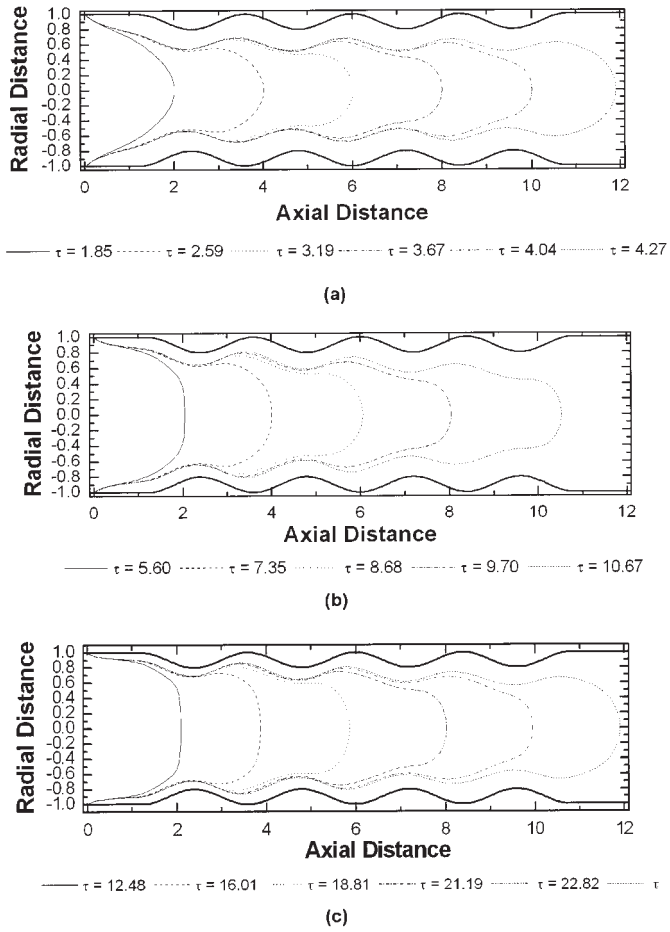


**Figure 13. Effect of Reynolds number on evolution of the free surface for (a) $Re_p = 10^2$, (b) $Re_p = 10^3$, and (c) $Re_p = 5 \times 10^3 \cdot (P_{ext}, \varepsilon^{-1}, R_{min}/R_{max}, n, \varepsilon_i, \varepsilon_e) = (8333, 12, 0.8, 4, 1.2, 1.2)$.**

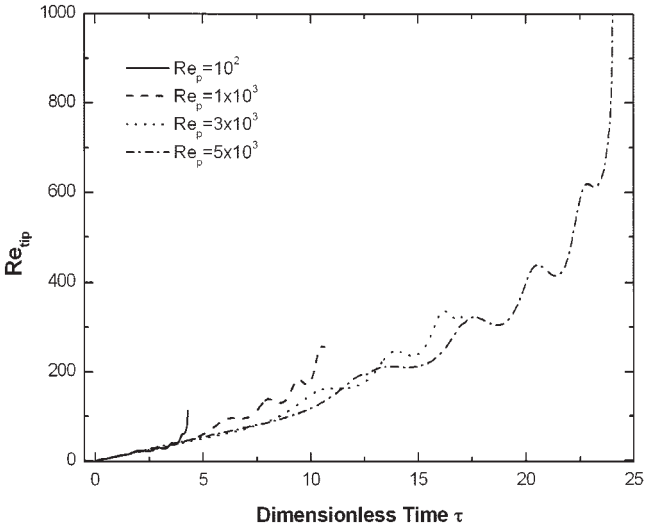


**Figure 14. Local value of $Re_{tip}$ at the fingertip as a function of the dimensionless time $\tau$, for ($P_{ext}$, $\varepsilon^{-1}$, $R_{min}/R_{max}$, $n$, $\varepsilon_i$, $\varepsilon_e$) = (8333, 12, 0.8, 4, 1.2, 1.2) and various values of $Re_p$.**

our simulations with $Re_p = 0$, irrespective of the values of the other parameters. This effect is repeated after the bubble passes through the other constrictions and is magnified as the bubble penetrates at longer distances. As a result, increasing $Re_p$ makes the width of the remaining film smaller in the introductory tube, but it keeps increasing along the axial distance. On the contrary, in the other two figures the effect of the increased is more apparent. Characteristically, for $Re_p = 5 \times 10^3$, the front of the bubble is so wide that the width of the remaining film at the first constriction is equal to 0.104 only, while the corresponding values for the other values of the Reynolds number are 0.261 ($10^2$), and 0.16 ($10^3$). These widths have been measured at long times, when the thickness of the film has reached its (asymptotic) minimum value as an equilibrium between the air pressure and the liquid normal forces has been established. Of course, increasing the Reynolds number breaks the symmetry in the deposited film. In fact, the bubble is still affected by the undulating wall, and the wavelength between the crests and troughs on its side surface is slightly smaller than the wavelength in the tube wall but seems to increase in the downstream direction (2.36 and 2.37 for the first two waves at $Re_p = 10^3$, vs. $\lambda = 2.4$). Since the arc length of the free surface has increased a lot and the originally introduced mesh points are not sufficient to resolve it, we increased the radial nodes to 100 in order to get converged solution in Figure 13c.

When we compare the snapshots from the three previous cases that correspond to equal displacements of the bubble tip, we conclude that increasing $Re_p$, increases the dimensionless time of the process, whereas the dimensional time actually decreases, due to the way we have nondimensionlized the velocity. Indeed the characteristic time $t_{ch}$, scales as $t_{ch} \sim (LR_{max}\rho/\mu)Re_p^{-1}$. Figure 14 depicts the evolution of the tip velocity, represented here by the local value of the Reynolds number, based on the bubble tip velocity $Re_{tip}$, for various values of $Re_p$. The nonzero value of the Reynolds number, allows the tip velocity to start from zero. $Re_p$ increases monotonically with time with some small amplitude oscillations, as the bubble tip goes through the tube constrictions. Because of its definition, the dimensionless velocity, $v$ is inversely proportional to $Re_p$. Therefore, although $Re_p$ increases significantly, $Re_{tip}$ depends weakly on it, because $Re_{tip} = Re_p v_{tip}$. Moreover, the particular values $Re_{tip}$ are smaller than the corresponding ones of $Re_p$ by a factor of 2–12 up to the time the bubble enters the exit tube. Even after the final acceleration, the final values of for each simulation are 113.04, 255.11, 340.33, and 417.3, clearly much smaller than the corresponding $Re_p$. This demonstrates that the velocity based Reynolds number increases with time, but always remains in the laminar regime. Each simulation seems to stop earlier although the bubble has nearly covered the whole tube in each case, because the characteristic time is inversely proportional to $Re_p$. Although the times do not correspond to equal axial penetrations of the bubble, they offer an indicative picture of the mean variation of each curve. Had we represented the tip velocity with $Ca_{tip}$, instead of $Re_{tip}$, we would have observed a strong increase of $Ca_{tip}$ with decreasing $Re_{tip}$, because $Ca_{tip} = P_{ext} v_{tip}$.

It is instructive to visualize the velocity distribution at high values of $Re_p$. To this end, we have plotted isolines of the axial and radial velocity components in discrete instances and at $Re_p = 3 \times 10^4$ (Figure 15). Despite this very large value of $Re_p$, a tip splitting instability does not arise in this geometry, as we had seen in a straight tube, even at the lower value of $Re_p \sim 4{,}000$, see Dimakopoulos and Tsamopoulos.[23,24] This is because the sequence of expansions and contractions of the bubble front do not allow it to develop a flat shape, which in

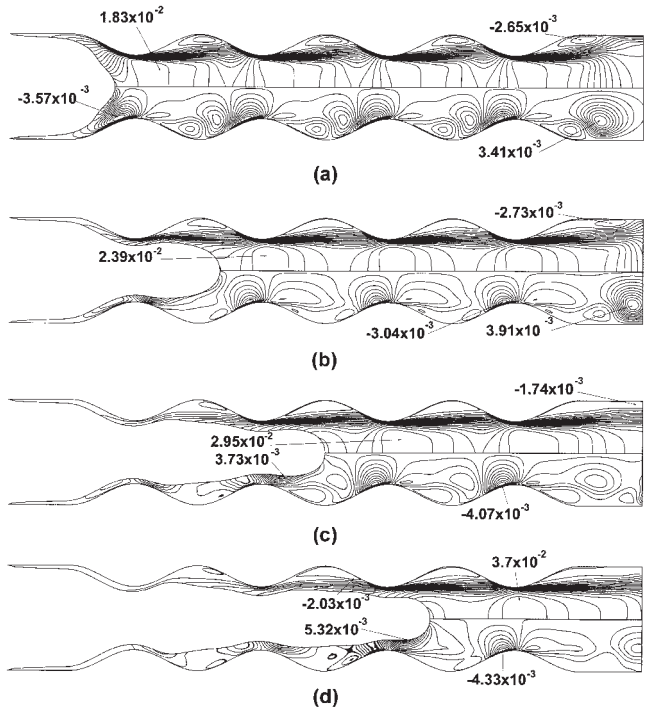


**Figure 15. Contour lines of the axial and radial velocity component, upper and lower part of each figure, in an undulated tube with $R_{min}/R_{max}$ = 0.6 at $\tau$ = 35.79, 43.53, 49.38, and 54.25. ($Re_p$, $P_{ext}$, $\varepsilon^{-1}$, $n$, $\varepsilon_i$, $\varepsilon_e$) = ($3 \times 10^4$, 8333, 12, 4, 1.2, 1.2).**

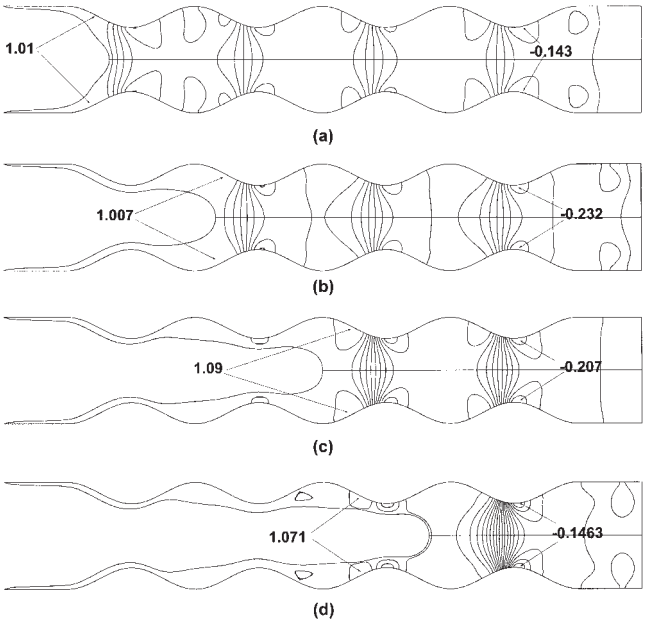


**Figure 16. Contour lines of pressure in an undulated tube with $R_{min}/R_{max}$ = 0.6 at $\tau$ = 35.79, 43.53, 49.38, and 54.25. ($Re_p$, $P_{ext}$, $\varepsilon^{-1}$, $n$, $\varepsilon_i$, $\varepsilon_e$) = (3 × $10^4$, 8333, 12, 4, 1.2, 1.2).**

combination with the accelerating flow would be susceptible to this instability. From the very beginning of the process ($\tau$ = 34.776) the flow field is completely different from the one we described in relation to Figure 2. The velocity does not have the two planes of symmetry within each undulation any more, but remains periodic between successive undulations with the exception of the undulation closest to the bubble tip. Moreover, the contour lines are strongly shifted in the flow direction. Starting with the axial velocity, we see that inside the tube expansions the velocity becomes negative closer to the wall. That is, a recirculation arises in these areas. The most intense recirculation develops inside the exit tube after the last constriction, and covers a large portion of this area. The axial velocity takes its minimum value there, which is equal to $-2.65 \times 10^{-3}$ at the first recorded instant. At the same time, the maximum axial velocity is equal to $1.83 \times 10^{-2}$, and is located at the first constriction ahead of the bubble tip. Additionally, there is a clear distinction of the axial flow field into three regions depending on whether the radial position is larger, approximately equal or smaller than $R_{min}/R_{max}$. As we have already mentioned, when $R > R_{min}/R_{max}$, flow recirculation is observed. In the second region, $R \sim R_{min}/R_{max}$, a shear layer arises with a strong velocity gradient in the radial direction, which spans the whole length of the tube. In the inner region $R < R_{min}/R_{max}$, the axial velocity varies slightly in the axial direction and even less so in the radial one, that is, it approaches plug flow. All three regions exist until the end of the simulation. Although the recirculations appear in all four snapshots and the area that they occupy is nearly time invariant, their magnitude changes with time. In all cases shown in Figure 15 $max(v_z)$ is located ahead of the bubble tip as the bubble is in the wider part of the tube, whereas at times not shown in this figure, and when the bubble tip is inside a constriction, the maximum axial velocity is located at the bubble tip. The position of the maximum radial velocity also varies with time. In the two first instants, it is located far downstream in the exit segment of the tube, while in the last two snapshots it appears, as is more common, on the side of the bubble surface. Another interesting point is that the negative regions of the radial velocity are located in the entrance of either the first constriction (Figure 15a) or all the constrictions ahead of the bubble (Figure 15b,c,d), because of the periodicity in the flow field. Generally, the radial velocity takes positive values in a larger portion of each undulation, and its variation is smoother there. In this largest value of inertia forces the bubble to avoid entering the wider part of the geometry, but to move in a more straight fashion with slight appearance of crests and troughs on its side surface. Throughout the simulation, the Reynolds number based on the maximum axial velocity is about two-orders of magnitude smaller than $Re_p$.

Figure 16 depicts the pressure distribution for the same flow parameters. It is noteworthy that always the maximum and the minimum values of the pressure are outside the range (0, 1). The position of the extrema is always on the tube wall, with the minimum located just after the last constriction and the maximum either at the entrance of the constriction at the level of or just ahead of the bubble tip, when this is located in the wider part of the tube (Figure 16b,c), or just behind it when it is in a constriction (Figure16a,d). The periodic pattern described for the velocity field is found here as well. The general clarity of this figure, depicting the most sensitive of the variables, the pressure, attests to the accuracy of our solution. The complete pressure distribution on the tube wall and at consecutive instances can be seen in Figure 17. Significant variations of the pressure take place throughout the tube. The most noteworthy of them is the small pressure increase within each wider portion of the tube and its exit. The increase especially in the exit is in contrast with the linear decrease, which appears at $Re_p$ = 0, compare with Figures 3 and 4. Cleary, the pressure now varies nonmonotonically in space and time. In the tube entrance, it is

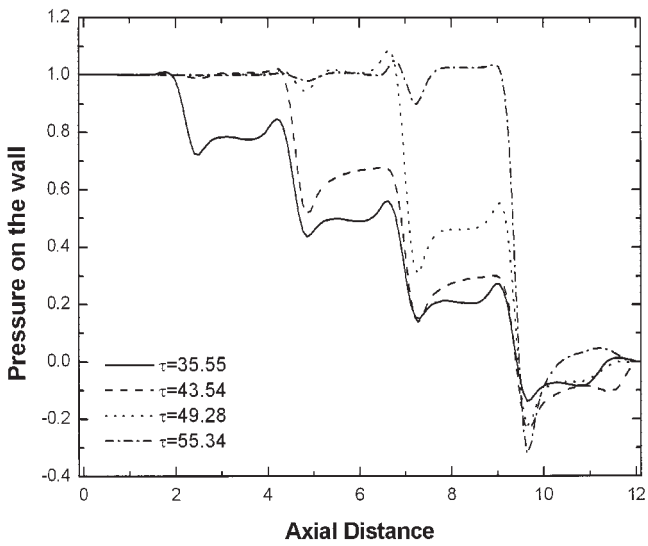


**Figure 17. Pressure distribution on the tube wall at various instances for ($Re_p$, $P_{ext}$, $\varepsilon^{-1}$, $R_{min}/R_{max}$, $n$, $\varepsilon_i$, $\varepsilon_e$) = (3 × $10^4$, 8333, 12, 0.6, 4, 1.2, 1.2).**

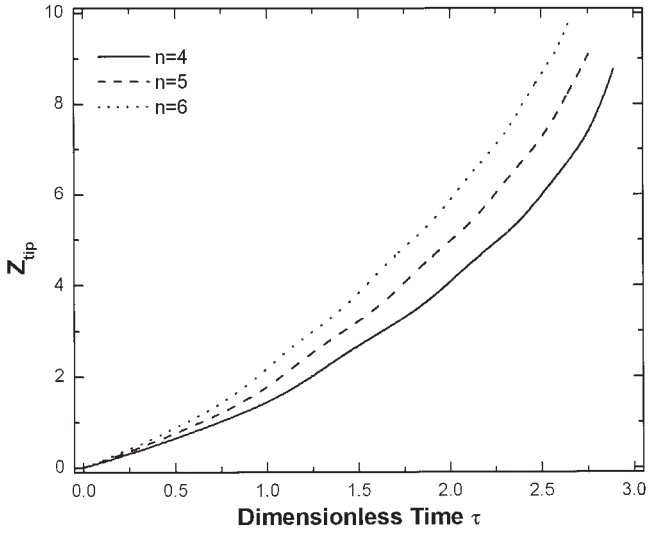


**Figure 18. Time evolution of the location of the tip for ($Re_p$, $P_{ext}$, $R_{min}/R_{max}$, $\varepsilon_i$, $\varepsilon_e$) = (0, 8333, 0.7, 1.2, 1.2), and different numbers of undulations.**

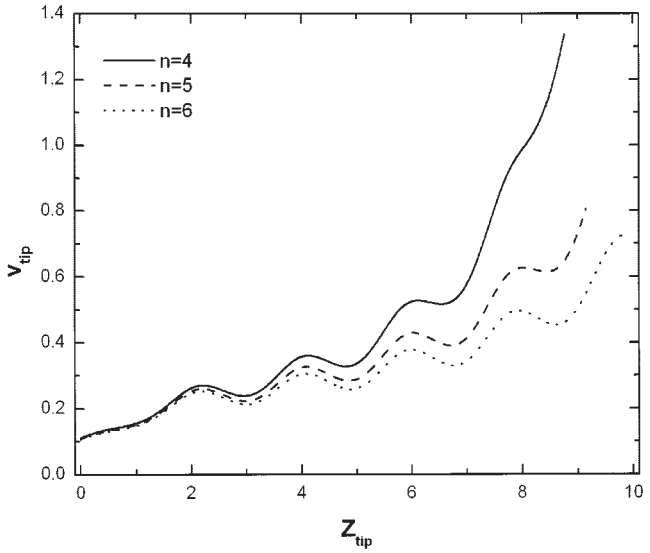


**Figure 19. Evolution of the tip velocity for different numbers of undulations ($Re_p$, $P_{ext}$, $R_{min}/R_{max}$, $\varepsilon_i$, $\varepsilon_e$) = (0, 8333, 0.7, 1.2, 1.2).**

$\sim$1 at all four instances. From the very first stages of the bubble evolution, just before each constriction, a large pressure drop occurs, followed by a wavy pressure variation after it. Their amplitudes are similar in each undulation at a given time instant. After the bubble front passes by a constriction, the pressure variation decreases there and the pressure slowly approaches 1. Necessarily, this is accompanied by an increase in the amplitude of the remaining waves and in the pressure jump after them. For example, at $\tau = 55.34$, two waves may be seen: the first one covers the tube length between 4.84 and 5.55 and the second one is longer, between 6.508 and 7.865. The difference between the maximum and the minimum amplitude of the former is equal to 0.031, while the corresponding difference of the latter is 0.148. The minimum value of the pressure at all times is located at $Z = 9.65$ and equals $-0.1369$, $-0.239$, $-0.225$, and $-0.32$ at times $\tau = 35.55$, 43.54, 49.28 and 53.34. The slope of the pressure jump in the last constriction increases monotonically with time and at $\tau = 55.23$ the pressure curve becomes almost parallel to the vertical axis.

### *Effect of the number of undulations*

First, we examined the effect of the number of tube undulations on the film thickness. To this end, we kept the dimensionless length of the introductory and the exit tubes constant, both equal to $\varepsilon_i = \varepsilon_e = 1.2$ and increased the number of undulations in the tube $n$, from 4 to 6, while $R_{min}/R_{max} = 0.7$. Each one of the undulations has length equal to $\lambda = 1.9$, and, consequently, the total aspect ratio changes from $\varepsilon^{-1} = 10$ to 11.9 to 13.8. Creeping flow conditions remain and a large pressure difference is applied $P_{ext} = 8333$. We observed that all three interfaces coincide, as long as the bubble front is well ahead of the examined tube section. This confirms once more that, under creeping flow, one can safely predict the film thickness using a single periodic segment of the tube and apply periodic boundary conditions between its ends.

The effect of the undulation ratio on the dynamic response of the tip location, its velocity and the pressure difference between the two ends of the liquid are shown in Figures 18, 19, and 20. In particular, in Figure 18 we observe that the evolution of the location of the tip exhibits small-amplitude oscillations, a direct consequence of the tube geometry, superimposed on a monotonic increase.[30] In addition, the time required for the bubble tip to reach a certain position in the tube increases or the bubble covers a longer distance at a given time as decreases or, equivalently, as the total length of the tube decreases. Although the pressure gradient would require the opposite, this indeed is the case, and it is readily explained considering that the char-

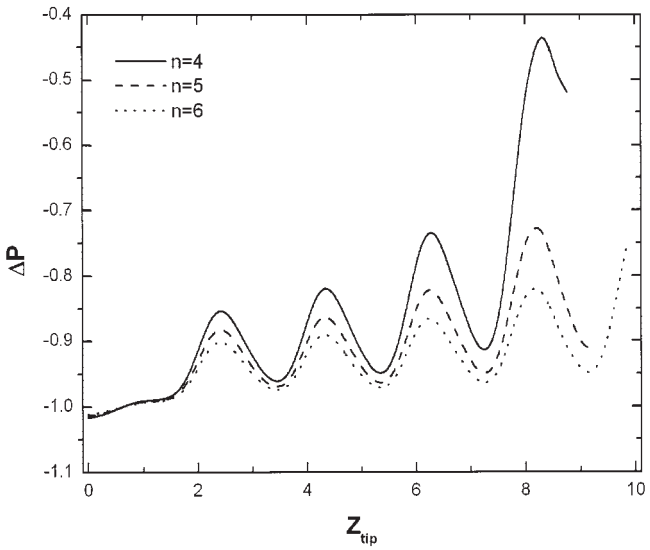


**Figure 20. Evolution of the pressure difference between the centerpoint on the outlet boundary and the bubble tip for different numbers of undulations. ($Re_p$, $P_{ext}$, $R_{min}/R_{max}$, $\lambda$, $\varepsilon_i$, $\varepsilon_e$) = (0, 8333, 0.7, 1.9, 1.2, 1.2).**

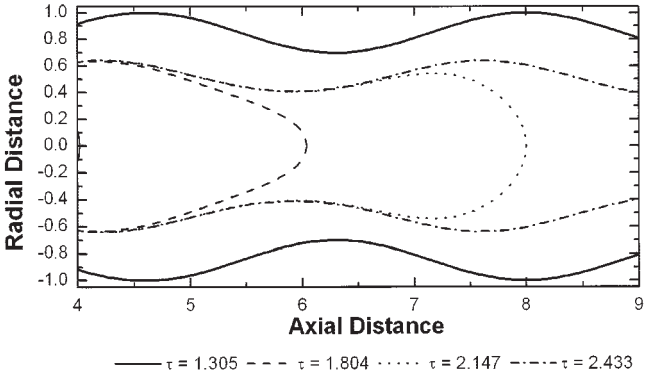


**Figure 21. Close ups of the bubble evolution in an undulated tube with n = 4, and $\varepsilon^{-1} = 16$ for ($Re_p$, $P_{ext}$, $R_{min}/R_{max}$, $\varepsilon_i$, $\varepsilon_e$) = (0, 8333, 0.7, 1.2, 1.2).**

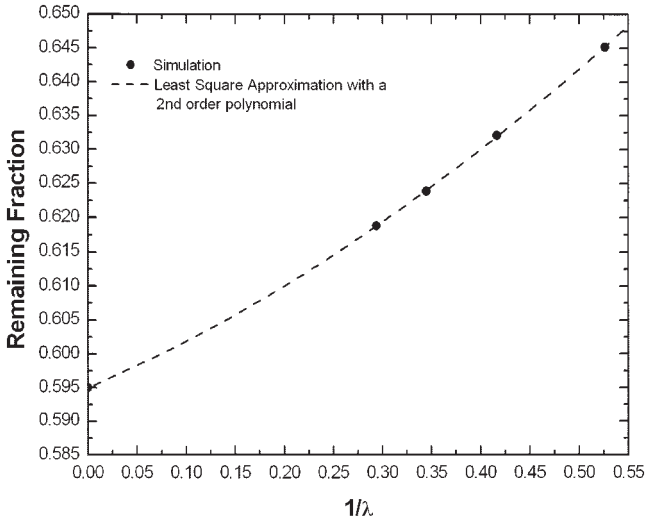


**Figure 22. Variation of the remaining fraction as function of the inverse undulation wavelength (1/λ) for ($Re_p$, $P_{ext}$, $R_{min}/R_{max}$, $\varepsilon_i$, $\varepsilon_e$) = (0, 8333, 0.7, 4, 1.2, 1.2).. Also shown is a best fit to the points by a second-degree polynomial $m_p = 0.595 - 6.24 \times 10^{-2}(1/\lambda) + 6.27 \times 10^{-2}(1/\lambda)^2$.**

acteristic time is proportional to $L^2$, leading to larger dimensional times as increases. Figure 19 shows that the three curves representing the evolution of the tip velocity deviate, especially at distances $Z_{tip} > 3$. Curves that correspond to $n = 5$ and $n = 6$ continue their evolution inside the tube for an additional undulation. Thereafter, the deviation between them becomes more apparent, but this is not included in this figure. Clearly, the local and absolute maxima in the velocity are always larger for $n = 4$, and quite interestingly there is a slight, but persistent shift of the locations of the maxima to the right as $n$ decreases. Similar effects can be observed in Figure 20, wherein the pressure difference $\Delta P$, between the bubble tip and the centerpoint of the outflow boundary is depicted. Here as well, the amplitude of the variation of $\Delta P$ increases as $n$ decreases. For the two cases with more undulations, this effect is not so intense and the growth rate is smaller, just because at the bubble tip for $n = 5$ and 6 there are still a number of undulations before the tube exit.

### *Effect of geometric wavelength*

Next, we examine the effect of the wavelength of each undulation on the displacement process. Figure 21 depicts a portion of the tube and the penetrating bubble at different instances with geometric parameters $n = 4$, $\varepsilon^{-1} = 16$, $R_{min}/R_{max} = 0.7$, and $\lambda = 3.40$, and flow conditions such that the effect of capillary and inertia forces is negligible $P_{ext} = 8333$ and $Re_p = 0$. The distribution of the remaining film, as well as the penetration of the bubble inside each undulation shares common characteristics with those in Figure 7. Calculating the remaining fraction as described earlier shows that the material that is deposited on the wall is now significantly decreased. In particular, for the current values of parameters $m_p = 0.619$, while for $\lambda = 1.90$ the approximate value of $m_p$ is *0.641*. In particular, Figure 22 shows that the remaining liquid fraction, defined by Eq. 20, increases almost linearly with the inverse wavelength of the tube undulations and, of course, as $\lambda^{-1} \rightarrow 0$ the remaining fraction approaches its value for a straight tube, 0.595.[8,23]

Information about the evolution of the tip location and its velocity for the same physical properties, and total dimensionless lengths varying from 10 to 16, because of variations in are shown in Figures 23 and 24. In particular, as the wavelength of tube undulation increases and, consequently, increases $\varepsilon^{-1}$, the dimensionless time that is required by the bubble to reach the exit of each tube increases as well. It is quite interesting that the dimensionless acceleration that is caused by the increase in the wavelength is more significant than that caused by increasing the number of undulations, although both result in about the same increase in $\varepsilon^{-1}$. This becomes apparent if we compare Figures 18 and 23. Characteristically, the distances that have been covered by the bubble within 2.5 units of dimensionless time for $\lambda = 1.90$, 2.40, 2.90, and 3.40 (or $\varepsilon^{-1} = 10$, 12, 14, 16) are 5.979, 7.551, 9.110, and 10.661. As we discussed

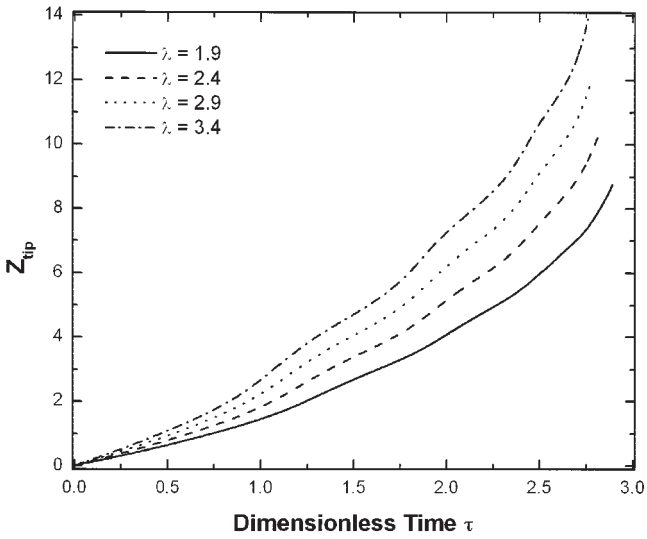


**Figure 23. Time evolution of the location of the tip for different undulation wavelengths and total lengths of the tube ($Re_p$, $P_{ext}$, $R_{min}/R_{max}$, $n$, $\varepsilon_i$, $\varepsilon_e$) = (0, 8333, 0.7, 4, 1.2, 1.2).**

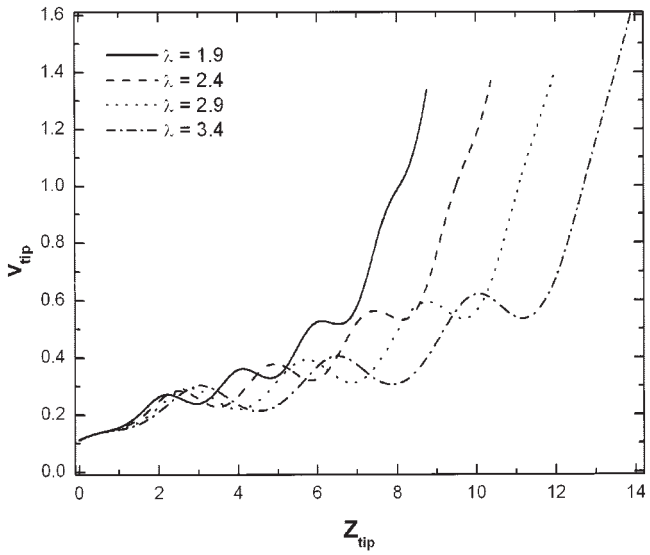


**Figure 24. Evolution of the velocity of the tip for different undulation wavelengths and total lengths of the tube ($Re_p$, $P_{ext}$, $R_{min}/R_{max}$, $n$, $\varepsilon_i$, $\varepsilon_e$) = (0, 8333, 0.7, 4, 1.2, 1.2).**

earlier, the dimensionless distance covered within the same time interval for $n = 6$, ($\varepsilon^{-1} = 13.8$, Figure 19) equals 8.642. Another way to understand this is by examining the evolution of the tip velocity (Figure 24); in particular, the distance between points that the tip velocity is maximized. For example, in the case of $\lambda = 1.90$, the axial distance between the two first maximum points is very close to the tube wavelength 1.901, while the axial distance between the third and the second local maxima is 1.998. If we examine the evolution curve for $\lambda = 3.40$, we will observe that the axial distance between the first two crests is 3.447, which is not as close to the tube wavelength as it was for $\lambda = 1.90$, and it increases further, since the distance between the third and second maxima is 3.554. In other words, increasing the wavelength of the tube decreases the resistance to the motion of the liquid, which does not exactly follow the wall geometry and can easier accommodate the tube undulations. Generally, the velocity curves are shifted to the right (because of the change in the length scaling) and down (because of the decreased resistance) as $\lambda$ increases. Studying the evolution of the pressure difference between the bubble tip and the centerpoint at the exit boundary, not included for conciseness, we observe a shifting of the curves to longer times and higher pressures as $\lambda$ decreases. Moreover, the amplitude of the periodic variations decreases as $\lambda$ increases. This is in agreement with the previous discussion and conclusions related to velocity.

### *Bubble break up*

While studying the displacement of a viscoplastic material from suddenly constricted tubes Dimakopoulos and Tsamopoulos[24] have demonstrated that inertia can lead to the development of air entrapments as the bubble tries to squeeze through the constriction and then expand in the narrower tube. On the other hand, while studying the effect of the ratio of the tube radii $S$, we have shown that decreasing it down to 0.2 created a gas jet with a very narrow radius just before each tube constriction. Decreasing $S$ further would lead to nearly isolated bubbles, one in each tube undulation. Therefore, it is natural to anticipate that the same effect could be generated by keeping at a low value and increasing the liquid inertia. This increase in $Re_p$ would allow the liquid to keep converging toward the axis of symmetry of the tube as it approaches the tube constriction and further decrease the neck of the air jet. This is indeed made clear by comparing the two cases with $Re_p = 0$, 1,000, in Figure 25. Here the same small undulation ratio is used, $R_{min}/R_{max} = 0.2$, while the rest parameters are ($P_{ext}$, $\varepsilon^{-1}$, $\lambda$, $n$) = (8333, 12, 2.4, 4). In both cases the bubble front becomes quite pointed when it tries to penetrate in the next geometric cell (for $Re_p = 0$ at $\tau = 37.96$, 58.22). As it starts emerging out of each constriction its front is flat, then it freely expands in both directions, but primarily in the radial one up to a maximum radius, which is significantly smaller than the radius of the tube at the given axial distance. In the entrance of each cell, the bubble develops a neck, which has a finite radius. It is clear that for all times, there is no tendency of the free surface, behind the advancing front, to move in the radial direction, that is, to increase or decrease the liquid mass that adheres to the tube wall at the constriction. On the contrary, for $Re_p = 1{,}000$ (Figure 25b), the radius of the bubble at the constrictions becomes progressively slightly smaller even when the bubble front is already approaching the next constriction. Table 4 summarizes the minimum values of the bubble radius at the three constrictions for these two values of the Reynolds number, calculated using least square fitting of fourth order polynomial. Details of the mesh for $Re_p = 0$ around the first constriction are shown in Figure 26. The snapshot corresponds to $\tau = 368.89$ or to an axial penetration of the bubble equal to

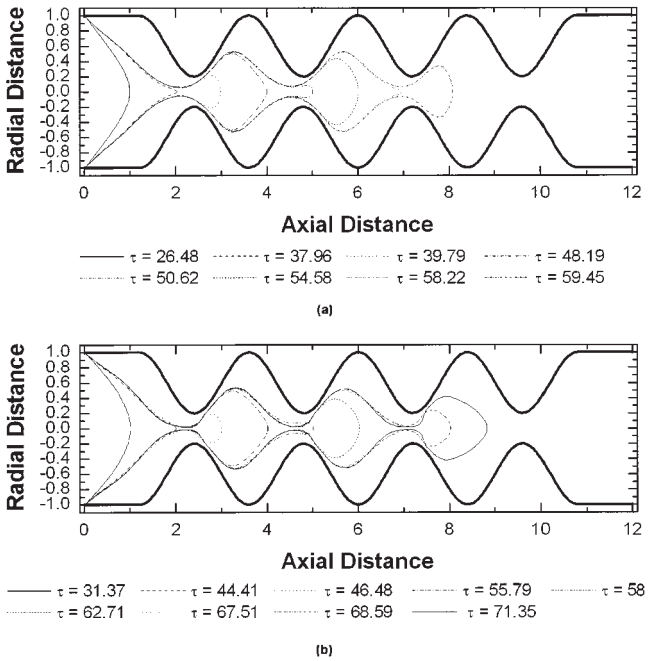


**Figure 25. Effect of inertia on the time evolution and the shape of the bubble for (a) $Re_p = 0$, (b) $Re_p = 10^3 \cdot$ ($R_{min}/R_{max}$, $P_{ext}$, $\varepsilon^{-1}$, $\lambda$, $n$, $\varepsilon_i$, $\varepsilon_e$) = (0.2, 8333, 12, 2.4, 4, 1.2, 1.2).**

Table 4. Location and Minimum Radius of the Bubble at the Three Tube Constrictions for ($P_{ext}$, $R_{min}/R_{max}$, $\lambda$, $n$) = (8333, 0.2, 2.4, 4) With and Without Inertia for Bubble Penetrations Corresponding to the Latest Snapshots Shown in Figure 26

| Minima / $Re_p$ | 1 | | 2 | | 3 | |
|---|---|---|---|---|---|---|
| | $R$ | $Z$ | $R$ | $Z$ | $R$ | $Z$ |
| 0 | 0.059 | 2.036 | 0.072 | 4.530 | 0.063 | 6.947 |
| 1000 | 0.011 | 2.147 | 0.018 | 4.572 | 0.005 | 7.111 |

2.0. For clarity, quadrilateral elements are shown, before they are split to create triangular elements. The flexibility and the robustness of the elliptic mesh generator are apparent, even for this most demanding case. Close ups of the mesh for this and other geometries generated by the same methodology, can be also found in [22].

The mesh we generated for the previous simulations had 80 radial and 140 axial elements. This gives accurate results up to the time shown, but it is not sufficient to follow the phenomenon for larger times as the bubble goes through more tube constrictions at higher Reynolds numbers. In such a case, it should be possible to follow the development of an isolated bubble in each cell. To this end, we increased the radial and axial nodes to 150 and 200, respectively, and the Reynolds number to $Re_p$ = 1,500, keeping constant the rest of the parameters. Figure 27 illustrates contour plots of the axial and the radial velocity, upper and the lower parts of the tube, at times $\tau$ = 48.64, 59.50, 72.06, and 76.37 which correspond to bubble penetrations equal to 2.02, 4.00, 8.00, and 11.00, when the simulations stop. As the bubble emerges from each constriction it inflates resembling a balloon, reaches a nearly ellipsoidal shape and then becomes pointed again as it tries to squeeze through the next constriction. Apparently, the increased inertia assists in the early development of nearly isolated bubbles inside each cell, which tend to inflate sequentially with the last one generating a new one in the next cell and feeding it with gas, and so on. The motion of the leading bubble continues due to the applied pressure on its front surface. As before, the maximum axial velocity appears either at the bubble tip or at the first constriction ahead of it. Negative values of the axial velocity, that is recirculating flow, appear on wide part of the expansion in each cell. This further intensifies liquid accumulation at the tube constrictions leading to a narrower neck. It is quite interesting to examine the film thickness on the wall. By closely comparing the previous plots, we observe that generally, the liquid-air interface follows the variation of the tube geometry, and the effect of the Reynolds number is nonmonotonic. This could be caused by the difference in the times (or bubble penetrations) that the different snapshots were taken. In particular, for the three values of $Re_p$ the axial penetrations are 8.07, 8.82, and 9.63, and for nonzero $Re_p$ there is some residual fluid flow from each cell to the constriction that is immediately after it.

Increasing the Reynolds number to even larger values, for example, $Re_p$ = 30,000 (recall that the velocity based Reynolds number is about 2 orders of magnitude smaller), the bubble neck at the first constriction becomes extremely low (R $\sim$ 0.0001), and one could safely assume that bubble break up takes place there (Figure 28b). However, we decided not to pursue this further at this point. The isolated bubble attains a bullet-like shape, having significantly smaller radius than its axial length even at earlier times, Figure 28a. Examining the second snapshot, we see that it elongates and simultaneously develops a wider back, which assists in its motion. Indicatively, the lengths of the isolated bubbles at times $\tau$ = 163.68, and 167.95 are 1.74 and 2.83, respectively. The velocity field shown in the same figure has more intense variation. This phenomenon of bubble formation, as a gas jet surrounded by a co-flowing liquid is forced through a constriction has been also

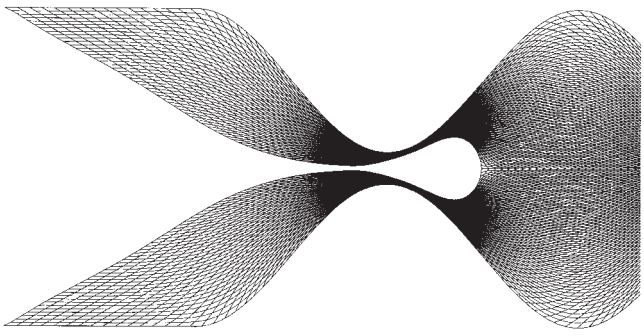

**Figure 26. Close up of the mesh around the first constriction, for an undulated tube with $R_{min}/R_{max}$ = 0.2 at $\tau$ = 368.89.**

($Re_p$, $P_{ext}$, $\varepsilon^{-1}$, $\lambda$, $n$, $\varepsilon_i$, $\varepsilon_e$) = (0, 8333, 12, 2.4, 4, 1.2, 1.2).

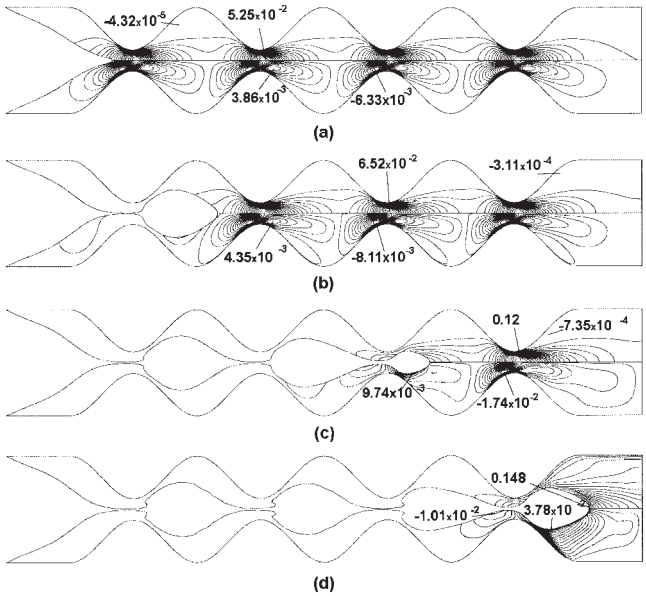


**Figure 27. Contour lines of the axial and radial velocity component, upper and lower part of each figure, in an undulated tube with $R_{min}/R_{max}$ = 0.2 at $\tau$ = 48.64, 59.50, 72.06, and 76.37.**

($Re_p$, $P_{ext}$, $\varepsilon^{-1}$, $\lambda$, $n$, $\varepsilon_i$, $\varepsilon_e$) = (1500, 8333, 12, 2.4, 4, 1.2, 1.2).

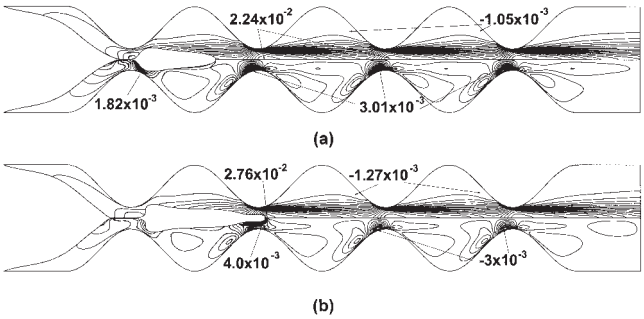


**Figure 28. Contour lines of the axial and radial velocity component, upper and lower part of each figure, in an undulated tube with $R_{min}/R_{max}$ = 0.2 at $\tau$ = 163.68, and 167.95.**

$(Re_p, P_{ext}, \varepsilon^{-1}, \lambda, n, \varepsilon_i, \varepsilon_e) = (3 \times 10^4, 8333, 12, 2.4, 4, 1.2, 1.2)$.

observed experimentally by a number of researchers.[43,44,45] In fact, various experimental arrangements have been proposed to fabricate perfectly monodisperse bubbles of controllable diameter and frequency by such a "flow focusing" mechanism. Of course, if this arrangement is to be used for generating a continuous stream of monodisprse bubbles, this should be accomplished within the tube by employing liquid inertia and other ideas reported in the references earlier. We plan to undertake such studies in the near future.

## Conclusions

We studied the transient displacement of Newtonian fluids from harmonically undulated tubes. We applied the quasi-elliptic grid generation scheme to create an optimal computational mesh in a highly deforming domain,[22] used the finite element technique, an implicit Euler method for the time integration and a decoupled iterative scheme for the solution of the set of nonlinear equations. Simulations show that at the creeping flow limit, the flow field in front of the bubble is nearly periodic in each geometric period. They are disturbed only when the bubble comes close to them. The variation of the remaining film is also almost periodic and increases as the ratio of the minimum to the maximum tube radii $S$ decreases. The maximum and the minimum cross sections of the free surface are located at axial positions, which do not coincide with those of the maximum and the minimum radii of the tube wall. Another interesting observation is the decreasing of the remaining fraction inside each undulation as the geometric wavelength increases or decreases, whereas it reaches the asymptotic value $\sim$0.60 at large values of $\lambda$ or as $S$ approaches 1. The evolution of both the tip and the exit velocity are affected by the magnitude of the undulation ratio. For small values of, the temporal response of the tip velocity tends to a delta function, while that of the exit velocity varies according to step function. Inertia breaks the symmetry of the flow and pressure fields, and causes recirculation of the fluid particles inside the expanding parts of the tube. The width of the film increases along the axial direction, because the bubble tries to follow a straighter way and avoid the large undulations of the tube wall. The undulating tube arrangement can produce monodisperse bubbles of well-controlled size at a desired frequency, a process with numerous important applications.

## Acknowledgement

This work was supported by the European Social Fund and National resources under the Pythagoras II program of the Ministry of Education of Greece.

## Literature Cited

1. Slattery JC. Interfacial effects in the entrapment and the displacement of residual oil. *AIChE J*. 1974;20:1145-1154.
2. Kreutzer MT, Kapteijn F, Moulijn JA, Heiszwolf JJ. Multiphase monolith reactors: Chemical reaction engineering of segmented flow in microchannels. *Chem Eng Sci*. 2005;60:5895-5916.
3. Otis DR, Johnson M, Pedley TJ, Kamm RD. Role of pulmonary surfactant in airway closure: a computational study. *J Appl Physiol*. 1993;75:1323-1333.
4. Dimakopoulos Y, Tsamopoulos J. Gas-penetration in straight tubes completely occupied by a viscoelastic fluid. *J Non Newt Fluid Mech*. 2004;117(2-3):117-139.
5. Tadmor Z, Gogos C. Principles of polymer Processing. John Wiley & Sons; 1979.
6. Washburn EW. The dynamics of capillary flows. *Physical Rev*. 1921; 17:243-283.
7. Fairbrother F., Stubbs AE. Studies in electroendosmosis. Part VI: The 'Bubble-tube' method of measurement. *Chem Soc*. 1935;1:527-529.
8. Taylor GI. Deposition of a viscous fluid on the wall of a tube. *J Fluid Mech*. 1961;10:161-165.
9. Cox BG. On driving a viscous fluid out of a tube. *J Fluid Mech*. 1962;14:81-96.
10. Cox BG. An experimental investigation of the streamlines in viscous fluid expelled from a tube. *J Fluid Mech*. 1964;20(2):193-200.
11. Kolb WB, Cerro RL. Role of pulmonary surfactant in airway closure: a computational study. *Chem Eng Sci*. 1991;46:215-232.
12. Bretherton FP. The motion of long drops and bubbles in tubes. *J Fluid Mech*. 1961;10:166-188.
13. Reinelt DA, Saffman PG. The penetration of a finger into a viscous fluid in a channel and tube. *SIAM J Sci Stat Comput*. 1985;6:542-561.
14. Park CW, Homsy GW. Two-phase displacement in Hele-Shaw cells. *J Fluid Mech*. 1984;139:291-308.
15. Goldsmitth HL, Mason SG. The flow of suspensions through tubes II. Single large bubbles. *J Colloid Sci*. 1963;18:237-261.
16. Teletzke GF. *Thin Films: Molecular theory and hydrodynamic implications*. University of Minnesota; 1983. PhD thesis.
17. Schwartz LW, Princen HM, Kiss AD. On the motion of bubbles in capillary tubes. *J Fluid Mech*. 1986;172:259-275.
18. Chen JD. Measuring the film thickness surrounding a bubble inside a capillary. *J Colloid Interface Sci*. 1986;109:34-39.
19. Ratulowski J, Chang H-V. Maragoni effects of trace impurities on the motion of long gas bubbles in capillaries. *J Fluid Mech*. 1990;210: 303-328.
20. Shen EI, Udell KS. A Finite Element study of low Reynolds number two-phase flow in cylindrical tubes. *J Appl Mech*. 1985;52:253-256.
21. Giavedoni MD, Saita FA. The axisymmetric and plane cases of a gas phase steadily displacing a Newtonian liquid-A simultaneous solution of the governing equations. *Phys Fluids*. 1997;9(8):2420-2428.
22. Dimakopoulos Y, Tsamopoulos J. A quasi-elliptic transformation for moving boundary problems with large anisotropic deformations. *J Comp Phys*. 2003a;192:494-522.
23. Dimakopoulos Y, Tsamopoulos J. Transient displacement of a Newtonian fluid by air in straight and suddenly constricted tubes. *Phys Fluids*. 2003b;15(7):1973-1991.
24. Dimakopoulos Y, Tsamopoulos J. Transient displacement of a viscoplastic material by air in straight and suddenly constricted tubes. *J Non-Newt Fluid Mech*. 2003c;112(1):43-75.
25. Dimakopoulos Y, Tsamopoulos J. Gas Assisted Injection Molding of fluids partially occupying straight or complex tubes. *J Polym Eng Sci*. 2006;46(1):47-68.
26. Pilitsis S, Beris AN. Calculations of steady-state viscoelastic flow in an undulating tube. *J Non-Newt Fluid Mech*. 1989;31:231-287.
27. Kouris Ch, Tsamopoulos J. Concentric core-annular flow in a circular

tube of a slowly varying cross-section. *Chem Eng Sci*. 2000;55:5509-5530.
28. Kouris Ch, Tsamopoulos J. Core-annular flow in a periodically constricted circular tube, I. Steady state, linear stability and energy analysis. *J Fluid Mech*. 2001;432:31-68.
29. Kouris Ch, Tsamopoulos J. Core-annular flow in a periodically constricted circular tube, II. Dynamics. *J Fluid Mech*. 2002;470:181-222.
30. Gauglitz PA, Radke CJ. Dynamics of Haines jumps for compressible bubbles in constricted capillaries. *AIChE J*. 1989;35:230-240.
31. Ryskin G, Leal LG. Orthogonal Mapping. *J Comp Phys*. 1980;50:71-100.
32. Christodoulou KN, Scriven LE. Discretization of free surface flows and other moving boundary problems. *J Comp. Phys*. 1992;99:39-55.
33. Tsiveriotis K, Brown RA. Boundary-conforming mapping applied to computations of highly deformed solidification interface. *Int J Num Meth Fluids*. 1992;14:981-1003.
34. Kouris Ch, Dimakopoulos Y, Georgiou G, Tsamopoulos J. Comparison of spectral and finite element methods applied to the study of the core-annular flow in an undulating tube. *Int J Num Meth Fluids.* 2002;39:41-73.
35. Löhner R. *Applied Computational Fluid Dynamics Techniques*, New York: John Wiley & Sons; 2001.
36. Soulaimani A, Fortin M, Dhatt G, Ouellet Y. Finite element simulation of two- and three-dimensional free surface flows. *Comp Meth Appl Mech Eng*. 1991;86:265-296.
37. Sani RL, Gresho PM. Resume and remarks on the open boundary condition minisymposium. *Int J Num Meth Fluids*. 1994;18:983-1008.
38. Papanastasiou TC, Malamataris N, Ellwood K. A new outflow boundary condition. *Int J Num Meth Fluids*. 1992;14:587-608.
39. Ruschak KJ. A method for incorporating free boundaries with surface tension in finite element fluid-flow simulators. *Int J Num Meth Eng*. 1980;15:639-648.
40. Poslinski AJ, Tsamopoulos JA. Inflation dynamics of fluid annular menisci inside a mold cavity-I. Deformation driven by small gas pressure. *Chem Eng Sci*. 1991;46(1):215-232.
41. Gresho PM, Lee RL, Sani RL. On the time-dependent solution of the incompressible Navier-Stokes equations in two and three dimensions. In Taylor C, Morgan K. *Recent Advances in Numerical Methods in Fluids*. Swansea, UK: Pineridge Press Ltd.; 1980:27-81.
42. Staples TL, Shaffer DG. Wicking flow in irregular capillaries. *Coll and Surf*. 2002;204:239-250.
43. Ganan-Calvo AM, Gordillo JM. Perfectly monodisperse microbubbling by capillary flow focusing. *Phys Rev Let*. 2001;87:274501-1.
44. Gordillo JM, Ganan-Calvo AM, Perez-Saborid M. Monodisperse microbubbling: Absolute instabilities in coflowing gas-liquid jets. *Phys Fluids*. 2001;13:3839-3842.
45. Garstecki P, Fuerstman MJ, Whitesides GM. Oscillations with uniquely long periods in a microfluidic bubble generator. *Nature Physics*. 2005;1:168-171.

*Manuscript received Nov. 15, 2005, and revision received Mar. 28, 2006.*